Biomaterials Science

REVIEW

View Article Online
View Journal | View Issue

Cite this: *Biomater. Sci.*, 2019, **7**, 1746

Current concepts in nanostructured contrast media development for *in vivo* photoacoustic imaging

Mirko Maturi, Erica Locatelli, Ilaria Monaco and Mauro Comes Franchini *

Photoacoustic (PA) imaging is indeed one of the most promising bioimaging techniques for theranostics applications in humans, allowing for the visualization of blood vessels and melanomas with high spatial resolution. However, in order to overcome the endogenous contrast arising from interfering endogenous species such as haemoglobin and melanin, specific contrast agents need to be developed, allowing PAI to successfully identify targeted contrast in the range of wavelengths in which interference from the biomatrix is minimized. This has been first performed by small molecule dyes, which, however, suffer from some important limitations such as low hydrophilicity and short circulation times. For this reason, scientific research has recently directed its efforts towards the development of nanostructured contrast agents capable of providing efficient PA contrast at low concentrations with low toxicity and high biocompatibility. The principal nanostructures are based on (1) metal and semiconducting nanoparticles, amongst which variously shaped nano-gold plays the main role, (2) carbon nanomaterials, such as carbon nanotubes and graphene, and (3) conjugated polymer nanoparticles. In this review, the principal characteristics of this class of materials are reported and greater focus is directed towards *in vivo* studies. A detailed analysis is performed on various physical–chemical parameters that define the PA response of reported contrast agents, like absorption coefficients and photoacoustic efficiencies. By comparing the experimental data, this review provides a comprehensive tool for the evaluation of new nanostructured contrast agents for PA imaging.

Received 9th November 2018,
Accepted 31st January 2019

DOI: 10.1039/c8bm01444b

rsc.li/biomaterials-science

Introduction

Photoacoustic (PA) imaging is an emerging technique based on the illumination of a specimen with NIR nanosecond-pulsed laser light and the absorption of photons by chromophores in the sample results in the generation of acoustic waves, which are then detected and processed to form an image. Thanks to acoustic detection, it is often possible to couple PA imaging to ultrasound (US) echographic systems: ultrasounds are directed to the sample together with the laser, scattered and diffused in the tissues and detected back by a separate US detector.[1] Although PA and US image formation and the factors that affect spatial resolution are mostly the same, the contrasts that generate the images are essentially different. A US image describes the acoustic impedance mismatch between different tissues: US contrast, therefore, depends on the morphological features of the tissues, while PA represents the initial pressure distribution produced by the absorption of a pulse of laser light. The capability to perform photoacoustic detection on non-transparent samples provides the possibility of exploiting it for spectral characterization of biologic tissues, for which traditional optical spectroscopic tools cannot be generally applied. The field of optoacoustics has rapidly grown in terms of development of instrumentation, image processing algorithms, *in vivo* application of the technique in clinical medicine and basic biological research.[2] In photoacoustic (PA) imaging, ultrasound waves are generated by irradiating tissues with modulated or pulsed laser light. For applications in biology and biomedicine, optical wavelengths in the near-infrared (NIR, 700–1500 nm) are applied due to the high transparency of tissues in this range, achieving penetration depths up to several centimeters. In this region of the electromagnetic spectrum are located the two so-called biological windows, in which the absorption from biological tissues is minimized (or transparency is maximized). Recently, PA imaging has emerged in biomedicine thanks to its easy translation in human studies and its remarkable features compared to most other imaging techniques. PA imaging allows for extremely high spatial resolution which is only limited by the tech-

Department of Industrial Chemistry "Toso Montanari", University of Bologna, Viale Risorgimento 4, 40136 Bologna, Italy. E-mail: mauro.comesfranchini@unibo.it; Fax: +051-2093654; Tel: +051-2093626

nological implementation of the ultrasonic transducer. With respect to traditional optical imaging (fluorescence or phosphorescence), PA imaging employs a much longer irradiation wavelength, with a consequent increase in penetration depth and in safety associated with laser employment. Moreover, the merging of light- and sound-based approaches allows for the evaluation of molecular spectral features of the analysed specimen together with its morphological details, to which ultrasounds are mostly sensitive. Although organic tissues can generate strong PA signals, the employment of specific contrast agents is desirable to retrieve detailed information, and most of the research activity has focused on this aspect.

Within the field of photoacoustics, the currently most exciting challenges are represented by the design and development of nanostructured contrast agents associated with increasingly higher contrast-to-noise ratios, little or no toxicity, and rapid clearance from the circulatory vessels. In addition, by moving the absorption of contrast agents to higher wavelengths, it will be possible to achieve much greater penetration depths and lower interference from endogenous chromophores. With this approach, PA is predicted to become an extensively versatile tool for diagnostics in medicine. With the present work, we aim to review the fundamental applications of nanostructured contrast agents for PA imaging of biological systems *in vivo*, with a particular focus on the peculiar properties that allow each of the different nanostructures to generate PA signals. First, the main physical–chemical properties of nanostructures will be examined, and then their PA performances will be compared and the most remarkable results shown.

Endogenous contrast

Standard implementations for PA imaging require laser-emitting light in the near-infrared window of the electromagnetic spectrum (λ = 800–2000 nm) since shorter wavelengths would be scattered and absorbed to a greater extent. Since NIR light can achieve high penetration depth in biological tissues of the order of several centimeters, part of the incoming photons will be absorbed by chromophores naturally present in the tissues such as lipids, water, collage, melanin and hemoglobin in its two forms, oxygenated (Hb) and deoxygenated (HbO_2); these are referred to as endogenous chromophores (Fig. 1a). Hemoglobin is an iron-based metalloprotein responsible for the delivery of molecular oxygen throughout the body: it undergoes structural and electronic modifications upon O_2 binding, which results in a modification of its absorption spectrum. This allows measuring the total hemoglobin concentration and oxygen saturation by multispectral PA imaging, which provides helpful information for the study of tumor angiogenesis.[5–9] It is also worth mentioning the absorption behavior of lipids at long wavelengths (930 and 1210 nm) related to the second overtone of the C–H stretching, which are abundant in fatty acid chains.[10,11] Contrast can arise from water if excited at 975 nm, whereas melanin, thanks to its intense absorption throughout the biological window, allows for the detection and characterization of primary melanoma and metastatic melanoma cells by PA imaging.[12] However, melanin strongly influences the penetration depth achievable with PA imaging, drastically limiting the performances of PA imaging in melanin-rich tissues. However, this can be exploited to employ melanin-based nanomaterials as exogenous contrast agents, after the required chemical modification.[13] Anyway, intrinsic chromophores only give access to a limited number of applications in biological processes. In PA imaging for biomedical applications, these absorptions represent the background that must be overcome by efficient contrast agent engineering capable of highlighting specific features of the investigated biological system. The absorption profiles of endogenous chromophores generate two distinct biological windows in the NIR between 650 and 950 nm and the second between 1000 and 1350 nm, separated by the strong absorption from lipids at 950–1000 nm (Fig. 1b). Even though endogenous contrast can be significantly relevant for particu-

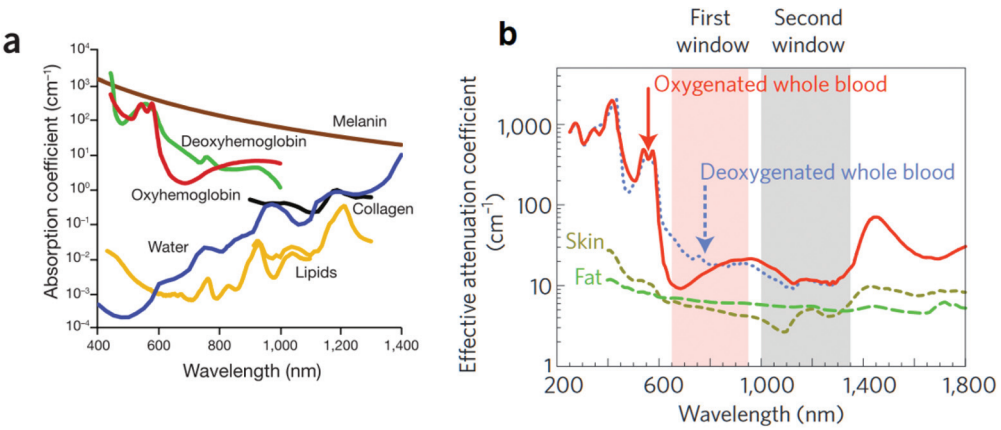

Fig. 1 Endogenous chromophores. (a) Absorption spectra of the main endogenous chromophores. At long wavelengths, the contribution of oxy- and deoxy-hemoglobin is negligible but the interference of water and fat is increasing. Melanin covers the whole spectral range, strongly reducing the optical penetration depth in melanin-rich regions. (b) Attenuation coefficients for oxygenated and deoxygenated blood, fat and skin, with the two biological windows highlighted. Adapted from ref. 3 and 4.

lar tissues or for particular excitation wavelengths, several multivariate analysis tools have been developed for the resolution of the spectral mixtures in PAI. For example, the implementation of multivariate curve resolution (MCR) algorithms for the decomposition of multispectral PA images in distribution maps of the single components of the endogenous PA contrast has been recently reported.[14,15] The multivariate separation of endogenous and exogenous contrast in PA imaging is yet to be explored, but this could make contrast-based PA imaging an important non-invasive diagnostic tool in the near future.

Contrast media for PA imaging *in vivo*

In 2017 the global contrast agent market size was valued at USD 4.89 billion and is anticipated to constantly grow (Fig. 2). Leading categories in the market are barium-based, iodinated, gadolinium-based, and microbubble contrast media: this is attributable to the preferential exploitation in the clinical approach of X-ray and CT procedures, as well as MRI procedures. However, these materials are currently under regulatory scrutiny, which is expected to prove detrimental for the market until the arrival of safer alternative agents. From the application point of view, neurological disorders account for the largest share, followed by cardiovascular disorders and cancer. High applicability of imaging modalities and accessibility to launched products for diagnosis of cancer or other diseases are strongly required from the actual market.[16]

As has already been discussed, the need for exogenous contrasts arises from the diffusion and non-specificity of endogenous PA-responding macromolecules. Although endogenous chromophores can provide useful information about blood flow, oxygen saturation and lipid content, they do not make PA suitable for the detection of specific diseases *in vivo*. Contrariwise, smartly-engineered nanostructured contrast media can be precisely designed for each particular application in diagnostics and, sometimes, as theranostic agents. In the present section, the most outstanding classes of exogenous contrast media for PA imaging will be presented together with their main physical–chemical properties. Firstly, molecular contrast performed by small molecule dyes will be briefly discussed, and then our focus will be mainly directed towards nanostructured contrast agents which are currently available in the literature.

Small molecule dyes

Small molecule dyes (SMDs) are polyconjugated organic chromophores; for application as PA contrast agents in deep tissues, absorption in the NIR is required. The optimal dye shows extended conjugation, which leads to the contraction of the HOMO–LUMO gap energies to energies corresponding to the near-infrared region of the electromagnetic spectrum: upon the absorption of NIR radiation, an electron of the dye is promoted from its HOMO to its LUMO, and relaxation of the excited states occurs *via* non-radiative processes (heat-wave), leading to anisotropic photoacoustic emission. Moreover, the fluorescence quantum yield of the dye should be as low as possible to maximize photoacoustic efficiency and contrast.[17,18] The brightest future for this class of PA contrast media is expected to be experienced by the FDA-approved indocyanine green (ICG) (Fig. 3a). It has a strong and characteristic concentration-dependent absorption band at around 800 nm in diluted solutions (Fig. 3d); it is water soluble and biocompatible and shows intense fluorescence emission in the NIR (around 850 nm) with low radiative quantum yield (2.7%).[19,20] Its improved photoacoustic performances have been attributed to the high lipophilicity of the molecule, which causes attraction between molecules by van der Waals interactions leading to extensive non-radiative relaxation of the excited states generated by laser light absorption.[21] The potential application as PA contrast agents of ICG, existing in the free molecular form or conjugated to specific targeting agents, has been widely investigated in recent years, showing high plasma protein binding and promising results as blood flow monitoring agents and providing good tumor contrast.[22–26] However, ICG suffers from some important drawbacks shared with most SMDs: poor aqueous stability, concentration-induced aggregation and quick clearance (around 2–4 min) from the body. In parallel, other classes of dyes have been explored as contrast

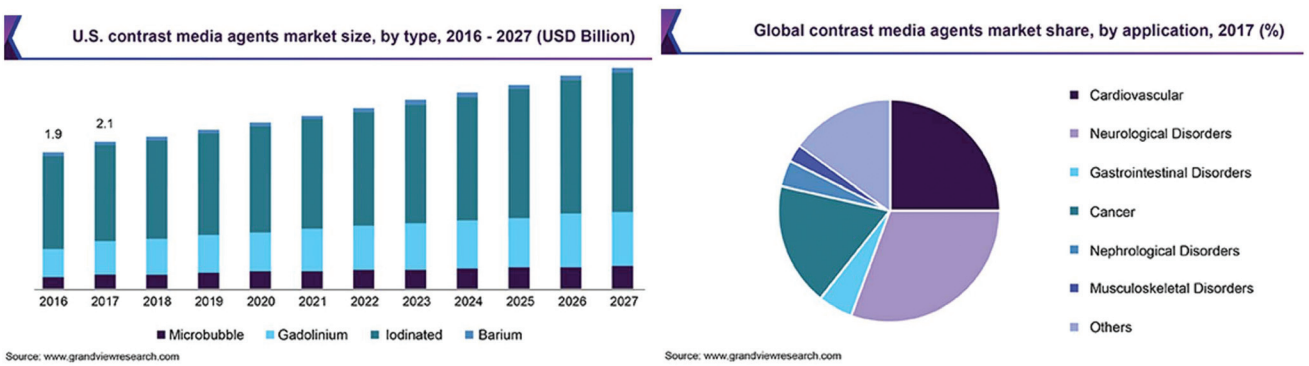

Fig. 2 Left: market size trends expected for contrast agents. Right: application of contrast agents in 2017. Adapted from ref. 16.

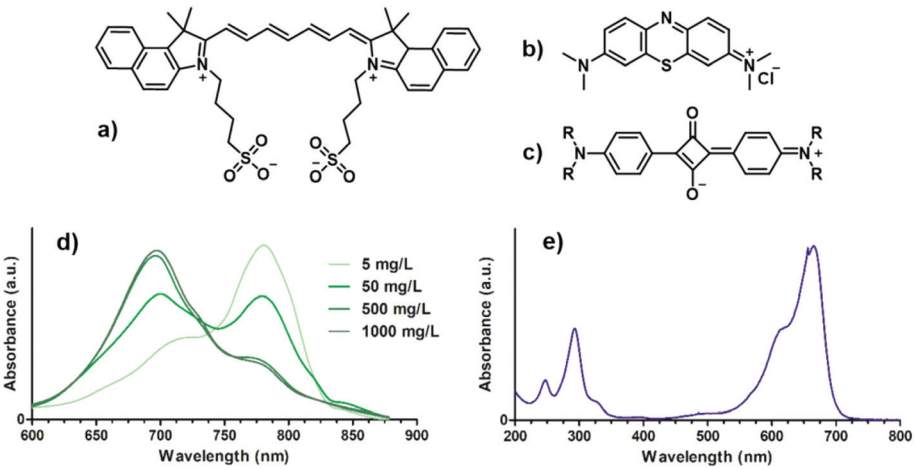

Fig. 3 Chemical structures of (a) ICG, (b) MB and (c) squaraine dyes, and UV-VIS spectra of (d) ICG at different concentrations and (e) MB.

agents for molecular PA imaging; amongst these, methylene blue (MB) has rapidly emerged thanks to its well-known biocompatibility and low photobleaching, together with its unique optical properties due to its strong absorption band centered at 664 nm (Fig. 3e), which may blue-shift with increasing concentration due to oligomerization equilibria.[27] The features of MB (Fig. 3b) have been recently exploited for several *in vivo* studies displaying good photoacoustic contrast *in vivo* after subcutaneous injection in mice for sentinel lymph node detection and photoacoustic imaging of the bladder, but due to the relatively shorter wavelength of the absorbed radiation, poor penetration depth can be achieved.[28–30]

Another representative class of SMD are squaraine dyes, characterized by an electron-deficient cyclobutene ring conjugated with two electron deficient groups (Fig. 3c); their optical properties can be tuned to the NIR region by adjusting the electron-donating strength of the conjugated groups.[31] Even though they show bright photoacoustic contrast due to their longer absorption wavelength and lower fluorescence quantum yield, their applications are limited by their intrinsic lipophilicity and chemical reactivity.

Since the most important requirement for an organic dye to be employed in PA is the NIR absorption, several different classes of small molecule dyes have been developed and studied in addition to the abovementioned compounds. Recently, appositely formulated naphthalocyanine dyes have been exploited as PA signaling compounds, aiming to image in the NIR with increasing sensitivity.[32,33] In addition, other dyes such as Prussian blue, Coomassie blue, BODIPYs (4,4-difluoro-4-bora-3a,4a-diaza-*s*-indacenes), porphyrines and cyanines have been explored for the purpose, showing good contrasts and sensing behaviour *in vivo*.[34,35,36–43,44] However, the development of new small molecule dyes as contrast agents for preclinical PA imaging is strongly limited by their molecular properties: the high conjugation degree required for NIR absorption drastically decreases the water-dispersibility properties of the dyes, leading to low stability in aqueous media and concentration-dependent optical properties. Moreover, no SMD capable of interacting with light waves longer than 800 nm has been reported, and their optical absorption coefficient is still quite low (<5000 M^{-1} cm^{-1}) compared to most nanostructured photoabsorbers. For these reasons, several methods have been developed recently for coupling ICG, MB and other dyes to a different set of nanostructures, like the encapsulation of dyes in biodegradable polymeric matrices such as PLA, PLGA and PLC, which can drastically increase their circulation lifetimes and their dispersibility in aqueous environments.[45,46]

While the encapsulation of dyes into polymeric micelles or liposomes has ensured the overcoming of some of their drawbacks, their coupling to metallic nanostructures (magnetic or semiconducting) has allowed for increased stability and imaging in multiple modalities.[47–49] The formulation of dye-conjugated nanosystems also allows for chemical functionalization with specific targeting moieties leading to increased specific local contrast.[50–57]

PA-responsive nanostructures

Photoacoustic-responsive nanostructures are composite nanomaterials capable of efficiently interacting with tissue-penetrating pulsed near-infrared light and to transform it into high-frequency ultrasound waves that can be detected by piezoelectric transducers to generate PA images. Their characteristics must include: (1) small size (<200 nm), allowing for good dispersion and active and passive tumor targeting;[58,59] (2) good biocompatibility and minimum cytotoxicity;[60] (3) high molar absorption coefficient in the NIR; (4) high photoacoustic efficiency and low fluorescence quantum yield; (5) low photobleaching.[61,62] In addition, by smart coupling of the photoactive core with other agents with specific activities, such as radiolabelled compounds, paramagnetic structures or fluorescence probes, multiple-modality imaging (PA-PET, PA-MRI, *etc.*) is allowed.[63] The main classes of nanostructures used as contrast agents for PA imaging are:

- Metal and semiconducting nanoparticles, whose optical properties are due to their metallic core (surface plasmon resonance or exciton absorption);

• Carbon nanomaterials, in which peculiar properties of nanostructured carbon allotropes are exploited to generate photoacoustic waves;

• Polymeric nanoparticles, composed of polyconjugated polymers or polymers containing photoactive groups such as porphyrin derivatives (HOMO–LUMO absorption).

Metal and semiconducting nanoparticles

In the field of nanomedicine, the role of transition metal nanoparticles (MNPs) has rapidly grown due to the characteristic properties that their compounds show at the nanoscale.[64] The optical properties of MNPs can arise from localized surface plasmon resonance (LSPR) in noble metal nanoparticles or from the formation of an exciton, an electron–hole pair, in semiconducting nanostructures. Also, their surface chemistry is relatively easy and well-known; therefore, it could be exploited for chemical functionalization with biocompatibilizing or targeting agents that need to be specifically developed for each application. The optical properties of MNPs mostly depend on their size and shape; thus, fine-tuning the parameters that determine the evolution of the morphology of the nanoparticle in the synthesis steps is a key factor for the obtainment of the desired properties in the final nanoconstructs. For this reason, MNPs show finely tunable absorption behavior in the NIR region of the electromagnetic spectrum, and experimental evidence reports much higher molar extinction coefficients compared to NIR dyes. Finally, their high thermal conductivity allows for improved conversion of the energy of the absorbed radiation into thermal waves.

Gold. In the last two decades, researchers have focused on the development of gold nanostructures due to their unique optical and physicochemical properties, their relative inertness and their prior use in humans. The optical properties of gold nanoconstructs arise from the LSPR phenomenon generated by the confinement of surface plasmons (coherent electron oscillations) in nanosized noble metal systems when they are hit by photons of light whose wavelengths are of the order of magnitude of the nanoparticle size. This leads to the absorption of the photon, whose energy is efficiently converted into a heat wave detectable by photoacoustic imaging. The energy corresponding to the LSPR phenomenon is directly connected to the maximum absorption wavelength of the particle, which is a function of several physical–chemical features including surface-to-volume ratio, polarization modes, shape and size.[65,66] By investigating the parameters that determine the position of the LSPR band, it is possible to tune the absorption maximum far from the visible to the NIR, making gold a very promising tool for generating photoacoustic signals by excitation in the NIR.[67] In addition, elemental gold can form very strong and almost-covalent bonds with thiol groups, with bond energies of the order of around 250–300 kJ mol^{-1}, enabling surface functionalization with polymers or small molecules bearing a thiol group.[68] Thiolated ligands can stabilize the high-energy surface of the nanoparticles by the formation of well-ordered self-assembled monolayers (SAMs) that can drastically increase the water stability properties of gold nanostructures and allow for the introduction of functional moieties for bioconjugation.[69] Even though gold is generally referred to as non-toxic, the pharmacokinetics of gold nanosystems is strongly dependent on their shape, size and surface functionalization, and a general evaluation of the toxicology of nano-gold cannot be made. Therefore, biocompatibility studies should be independently conducted *in vivo* or *in vitro* for each nanoconstruct that is developed for applications in nanomedicine.[70] Spherical gold nanoparticles (AuNPs) can hardly find applications in imaging due to their absorption behavior limited to the visible region of the electromagnetic spectrum, where tissue penetration is drastically limited by absorption and scattering from the skin layer (Fig. 4a). The surface plasmon peak red-shifts upon the increase of particle size: controlled aggregation of small NPs can give rise to micrometric clusters capable of efficiently interacting with NIR light, allowing for photothermal therapy and photoacoustic imaging in living mice.[71–74] However, the assembly size strongly reduces the possibility of accumulation in extravascular targets, only allowing for intratumoral rather than systemic injection.[75,76] Alternatively, their LSPR can be red-shifted by coating with strong absorbers such as melanin, strongly increasing PA signal and contrast.[77] In addition to AuNPs, gold nanorods (GNRs) display a characteristic localized surface plasmon along the longitudinal direction of the structure, which generates a sharp and intense low-energy absorption band (Fig. 4b).[78–81] This can be tuned up to the NIR by adjusting the aspect ratio of the rod, defined as its length-to-width ratio, with much higher optical absorption coefficients compared to organic dyes; this allows for strong contrast far from the regions of maximum absorption of endogenous chromophores.[82–87]

Besides, due to their larger size, they can accumulate *via* the enhanced permeability and retention (EPR) effect, allowing for passive tumor targeting.[88–91] However, their high surface-to-volume ratio makes them poorly photostable, and they tend to reduce their aspect ratio upon absorption, generating the need for a shell of dielectric material to improve the photostability of the structure.[92–95]

The optical behavior of nanoshells has been recently described, in which a continuous or semi-continuous layer of gold is deposited on a nanoparticle of a dielectric material.[96,97] The nanoshell thickness and radius can be tuned to make it capable of absorbing light in the NIR with extremely high extinction coefficients and improved photostability, allowing for PA contrast at low concentrations.[98] Also, the dielectric core material can be chosen to provide the nanoconstruct with additional features such as piezoelectricity and paramagnetism, allowing for applications in photothermal therapy and dual-modality imaging.[99,100] In 2005, Millstone *et al.* first reported the synthesis of small triangular gold nanoprisms which exhibit strong in-plane quadrupole plasmon resonance, resulting in an additional LSPR band at long wavelengths (1200–1400 nm) exploitable for applications in PA imaging.[101] Later, the same authors reported the implementation of their synthesis technique, which has then allowed for fine-tuning of

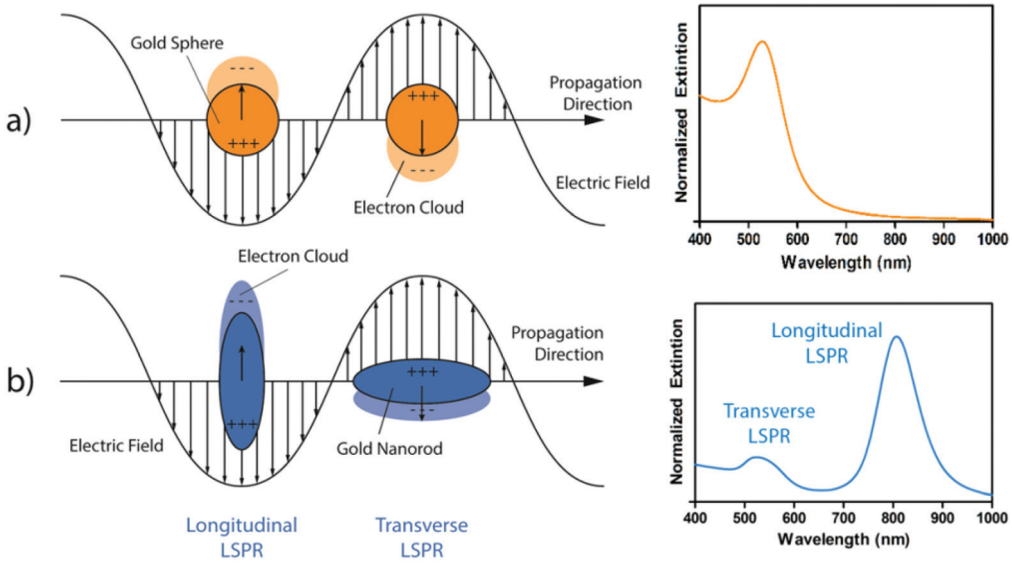

Fig. 4 Dipolar surface plasmon resonances and typical UV-VIS spectra of (a) AuNPs and (b) GNRs.

the prism edge length and therefore of the quadrupolar LSPR band position.[102] The electric field enhancement at the sharp edges of the nanoprisms leads to higher molar extinction coefficients compared to most other gold nanostructures, allowing for the PA imaging of living tissues with strong contrast signals.[103–105]

Gold nanocages show similar optical properties and can be used for drug or dye entrapment and controlled delivery, making these systems highly advantageous for molecular photoacoustic imaging.[106–108] They are generated by the galvanic displacement of Ag atoms on the surface of silver nanoparticles of various shapes in the presence of gold precursor salts, leading to hollow gold nanostructures with tunable optical properties in the NIR, suitable for use as PA contrast agent *in vivo*.[109–111] Moreover, gold nanostars have been recently reported to show characteristic absorption, which can be tuned in the NIR by controlling the size of the nanoparticle and the sharpness of its protuberances.[112,113] Nanoscale gold multipods, which are highly branched gold nanostructures similar to gold nanostars, have shown good optical properties in the near-infrared but little tunability.[114,115] Therefore, their applications as contrast agents for PA imaging are promising but still quite limited. Fig. 5 presents characteristic TEM images for different morphologies of gold nanostructures from

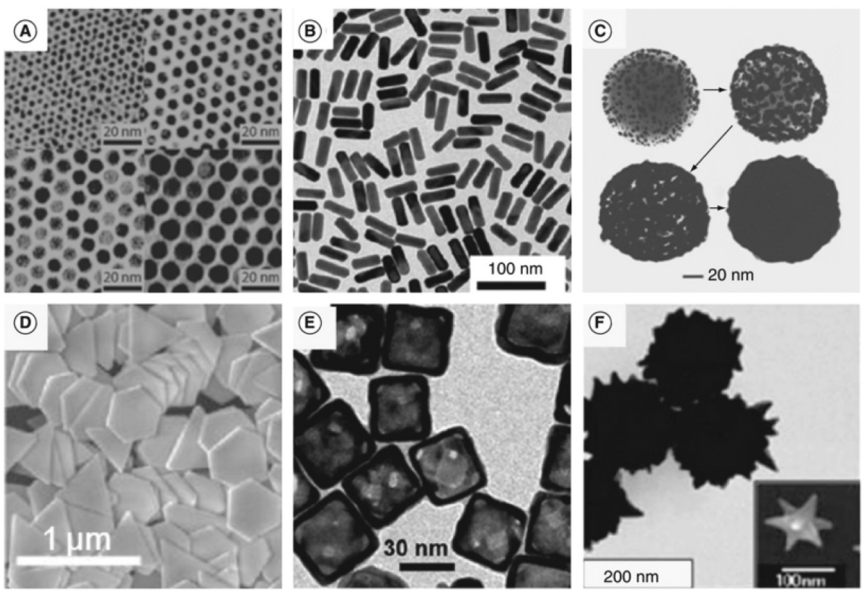

Fig. 5 Transmission electron micrograph of (a) gold nanoparticles, (b) gold nanorods, (c) gold nanoshells, (d) gold nanoprisms, (e) gold nanocages and (f) gold nanostars. Adapted from ref. 67.

the literature. Extensive work for the manipulation of gold at the nanoscale has recently led to the development of increasingly complex architectures with exotic shapes, which exploit sharp edges to red-shift their SPR absorption up to the NIR.[116,117]

Quantum dots. Semiconducting nanoparticles (or quantum dots, QDs) have found extensive application as fluorescent probes due to their small size and interesting optical properties, which can be tuned to the NIR by choosing the appropriate particle size. Since their dimensions are close to or smaller than their exciton Bohr radius, the spatial confinement of the electrons in the nanostructure results in an increased gap between valence and conduction bands and in a size-dependent splitting of the continuous energy band into discrete energy levels. Semiconducting nanoparticles have shown great potential for use as contrast agents for optical imaging due to their relatively easy synthesis and functionalization and their tunable fluorescence properties (Fig. 6).[118–120] The applicability of QDs as photoacoustic imaging contrast agents is guaranteed by their high absorption cross-sections (as high as 106 M^{-1} cm^{-1}), increased photostability after prolonged irradiation and quantum yield comparable with most small molecule dyes.[121] Thanks to QDs' optical properties, their *in vivo* applications have been widely explored in the literature, mostly focused on PA and fluorescence imaging.[122–125] However, still great effort needs to be directed towards the investigation of QD's pharmacokinetics (bioaccumulation, biodistribution, *etc.*) and toxicity before the application of these nanosystems in clinics.

Other metals. Even though gold nanostructures represent the most widely investigated metallic cores as contrast media for PA imaging due to their unique optical properties and chemical inertness, other nanostructured metals have been recently exploited to image biological tissues. Either exploiting localized surface plasmon resonance phenomena or semiconducting band gaps, metal nanostructures ensure low radiative quantum yields, increased photostability and good biocompatibility. Amongst these, antimony, bismuth, cobalt, copper, palladium, silver, titanium, tungsten and uranium nanoparticles with various shapes have shown great contrast with high photoacoustic response *in vivo* recently, but their toxicity and end-of-life are yet to be fully examined before they can find applications in clinics.[126–134]

Carbon nanomaterials

Carbon nanomaterials are classified based on their dimensionality, *i.e.* the number of spatial dimensions in which the nanostructure develops in space:

- 0-dimensional (0D): fullerene, carbon dots and nanodiamonds
- 1-dimensional (1D): carbon nanotubes
- 2-dimensional (2D): graphene

As is true for most nanostructured materials, the optical properties of carbon-based nanostructures are strictly dependent on their shape and size. Carbon nanomaterials are generally black, owing to a broad absorption in all the visible and NIR, but the phenomena that generate absorption are different in each case.[135] Fullerenes (0D) behave more as molecules than as nanostructures since their photophysical behavior in the visible is related to the HOMO–LUMO transition of one electron upon the absorption of a photon with the right energy. Since they have poor fluorescence properties, they are good candidates for the generation of high-frequency acoustic waves.[136]

However, their photostability is strongly limited: upon the absorption of NIR laser light, functionalized fullerenes gene-

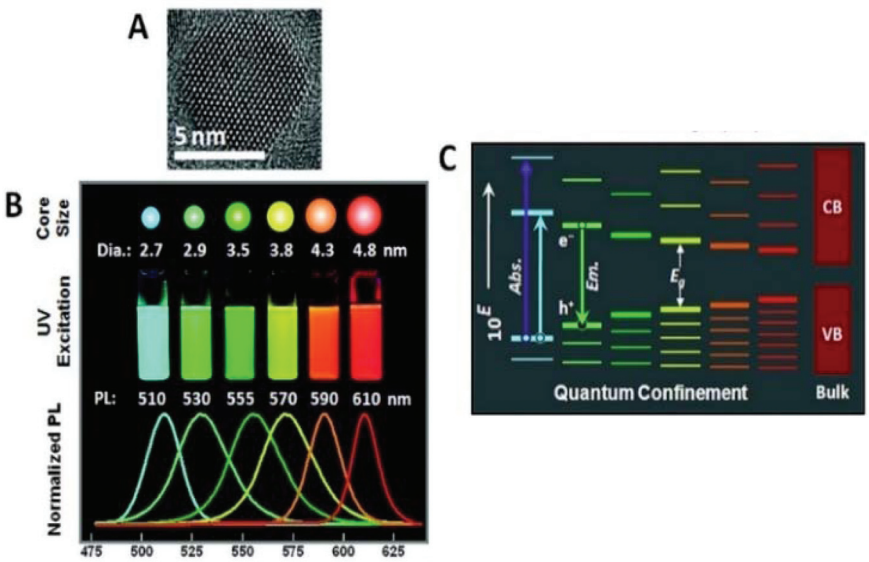

Fig. 6 (a) TEM images of CdSe/ZnS QDs; (b) photograph of QDs of different diameters exposed to UV light (365 nm) and their corresponding emission spectrum; (c) representation of the exciton energy levels as a function of the size of the QD. Adapted from ref. 120.

rate acoustic shock waves detectable by PA imaging, which disrupt the spherical structure of the molecules and their optical behavior.[137] On the other hand, carbon nanotubes (1D) owe their absorption properties to their semiconducting band gap, which may vary depending on the nanotube diameter and the chiral wrapping angle which describes how it has been constructed by a graphene sheet.[138] They also display fluorescence if isolated in micelles, but their photoacoustic response is stable enough to ensure a good photoacoustic response *in vivo*.[139–141] Moreover, graphene (2D) has been reported to be a gapless semiconductor; thus it would show weak absorption features in the NIR. However, due to the abundance of surface heterogeneities, graphene oxide (GO) shows strong absorption and fluorescence in the NIR (Fig. 7).[142,143] The exact origins of this behavior is still under debate, but it is believed to be related to the electronic transition at the boundaries between GO and non-oxidized sp2 graphene domains.[144,145] Due to their promising optical features and their easy surface functionalization and biocompatibilization, GO and graphene-based nanomaterials have widely shown their potential as contrast media for PA imaging, allowing for efficient imaging of cancer in multiple modalities.[146–148] Eventually, nanodiamonds are carbon nanoparticles in which all the atoms are sp^3 carbons and no graphitic-carbon is present. Their optical features include strong absorption and weak fluorescence, which arise from local defects in their microcrystalline structure generally induced by other elements like nitrogen.[149] On the whole, carbon nanomaterials have shown remarkable results but their absorption in the NIR is relatively broad, thus presenting an important challenge for spectral unmixing and distinction of the contrast from the background; this can be limited by contrast enhancement from NIR dyes attached to the carbon backbone.[150–153] Still great effort needs to be directed towards the comprehension of the overall photophysical behavior of carbon nanomaterials: their limited extinction coefficients and low biocompatibility make them only superficially explored contrast agents for *in vivo* photoacoustic imaging.

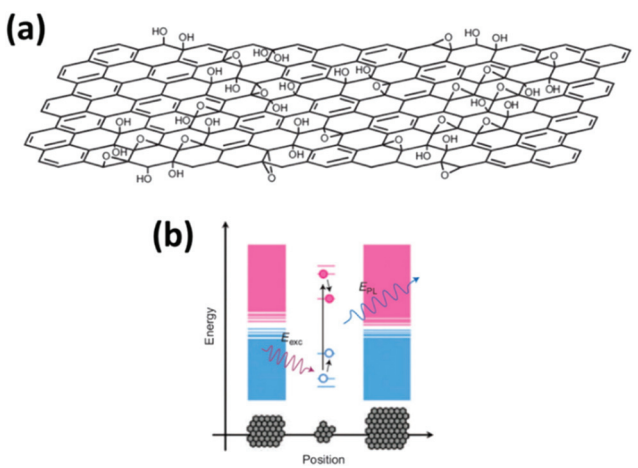

Fig. 7 (a) Proposed 3D structure of GO and (b) proposed energy band diagram of GO: larger band gaps are associated with smaller aromatic domain size. Adapted from ref. 143.

Polymeric nanostructures

Polymeric nanoparticles (PNPs) have found application in drug delivery due to their high biocompatibility and their ability to encapsulate and protect in their interiors drugs, dyes, proteins, *etc*.[154] In photoacoustic imaging, the most popular polymeric structures contain either conjugated polymers (CPs) or porphyrin-related units capable of directly interacting with NIR light thanks to their elevated π-conjugation spread throughout the whole polymer chains.[155] CPs are often referred to as semiconducting polymers (SPs), since their incredibly high conjugation degrees cause the formation of band structures and a massive shrinking in the gap between the π and π* bands, which resembles the features of most inorganic semiconductors.[156] By means of microemulsion or nanoprecipitation, CPs are able to self-assemble into nanostructures which are stable and well dispersible in water, known as conjugated polymer nanoparticles (CPNs) or semiconducting polymer nanoparticles (SPNs). Although their extinction coefficients are still lower than the ones of AuNPs and their absorption peak is broad, their high photostability and chemical versatility allow for both specific targeting and attachment of therapeutic moieties. CPs are macromolecules with a conjugated π-system spread throughout the polymeric backbone, and the polymers are densely packed to form nanoparticles with much stronger extinction coefficient and higher photostability compared with small molecule dyes. Optical properties, strictly connected to the polymeric core, can be tuned *via* modification of the polymeric backbone, combination of different polymers and control over aggregation and surface functionalization.[157–160] Because this class of contrast agents is still relatively young, detailed biocompatibility studies aimed at showing their potential for preclinical photoacoustic imaging still need to be conducted.[161–167] Principally, semiconducting polymers employed for PA imaging are composed of diketopyrrolopyrrole, phenothiazine, cyclopentadithiophene, fluorene, pyrrole or thiophene monomeric units, allowing for the structural rigidity required for efficient π conjugation (Fig. 8).[168–171] Finally, non-absorbing polymeric micelles can be employed for the encapsulation of PA active species such as lipophilic NIR dyes and complex structures, like perylene diimide derivatives.[172–178]

Essential parameters

In the process of PA contrast agent development, some key parameters should necessarily be taken into account to allow for clear comparison amongst different nanostructures.

• One of the most important parameters is ε or σ, the molar absorption coefficient or absorption cross section. The first one is the most often reported and it represents the portion of absorbed photons with a specific wavelength in a solution with unitary concentration, and it can be directly

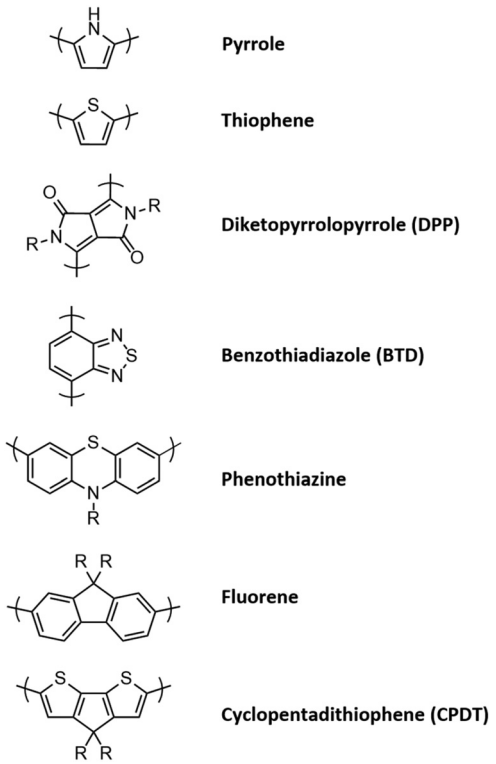

Fig. 8 Monomeric units principally employed in semiconducting polymers for PA imaging. The R residues can be aliphatic, to reduce close packing of the polymers chains, or aromatic, to increase the macromolecular conjugation degree.

used to compare different contrast agents; for example, gold nanostructures display ε between 10^9 cm^{-1} M^{-1} and 10^{11} cm^{-1} M^{-1} but most small molecule dyes have $\varepsilon \approx 10^5$ cm^{-1} M^{-1} and for SWNTs $\varepsilon \approx 10^6$ cm^{-1} M^{-1}.

• A second important parameter is η, the photoacoustic conversion efficiency, which represents the fraction of photons effectively converted into thermal energy. It is not reported often in the literature, but it completes the information given by ε since only photons which are efficiently absorbed and converted can give rise to PA signals. As reported in Table 1, some reference values for η are 23% for GNRs, 41% for Sb NRs and 48% for TiN nanoparticles.

• The PA performances of nanostructures are often summarized in the signal enhancement by the contrast agent compared to pre-injection signals. This approach allows comparing the brightness of the contrast agent directly to the surroundings, removing the influence of experimental variables, such as the type of tissue or the specific instrumentation employed.

• The size of the nanostructured contrast agent generally plays a key role in determining their optical properties but also whether accumulation *via* EPR is possible or not.

• Even though the toxicity and the long-term effect of systemic injection of nanostructures in living animals are rarely investigated in preclinical studies, *in vitro* biocompatibility and non-cytotoxicity studies are most often conducted prior to *in vivo* experiments. Minimum or no cytotoxicity must be observed for a nanostructure to be considered as a candidate for PA imaging at the clinical and preclinical levels.

• Usually, the maximum absorption wavelength of the nanoconstruct and the excitation wavelength employed in PA imaging should be as close as possible to maximize the absorption of photons and thus the PA signal. As has already been mentioned, both wavelengths should fall in the biological windows of the NIR region (650–950 nm and 1000–1300 nm) to reduce endogenous contrast and to maximize penetration depth.

• Finally, the injection dose is clearly useful to compare the strengths of PA contrast *in vivo*, together with the time required for contrast accumulation. It should be evaluated considering toxicity, PA performances *in vitro* and whether the accumulation is expected *via* active or passive targeting.

Moreover, some novel multifunctional contrast agents allow for imaging in multiple modalities; this can be done either by covalent binding different components, each with its own contrast ability, or by employing compounds which are intrinsically responsive to multiple imaging techniques, allowing for unambiguous contrast detection. Finally, some of the most promising nanostructured contrast agents display activatable PA activity: contrast can only be observable when some chemical modification of the nanocomposite structure triggers the PA emission by the sonophore.

In Tables 1–3, the most important parameters are reported for a variety of nanostructured contrast agents implemented in *in vivo* PA imaging.

In vivo applications

In this section, the recent applications of the previously described nanostructured contrast media are highlighted. Herein, we took into consideration only the most significant results of *in vivo* experiments. Firstly, the most remarkable preclinical results obtained with molecular contrast agents are rapidly summarized, and then each class of nanostructured contrast agents is thoroughly investigated.

Small molecule dyes

In 2010, Kim *et al.* reported how ICG could help in the identification of sentinel lymph nodes (SLNs) and their surrounding vessels for breast cancer early diagnosis.[179] To prove this, 5 rats underwent PA imaging *in vivo* after the injection of 1 mM ICG solution. SLNs were clearly visible in the PA images obtained, with a 6-fold signal enhancement recorded compared to the system before injection. In addition, ICG fluorescence was exploited for dual-modality imaging, leading to the formulation of fluorescence images that were matching the PA results. Later, in 2018, Wilson *et al.* employed antibody-conjugated ICG for intraoperative photoacoustic and dual fluorescence imaging of breast cancer to help the surgeon during the removal of tumoral tissues for minimizing positive resection margins.[180] In 2015, Garcia-Uribe *et al.* employed methylene blue for the same application in a clinical trial on

Table 1 Summary of the physical–chemical properties of gold nanostructures as *in vivo* PA contrast agents in the recent literature

	Targeting/coating	Size [a] (nm)	Absorption (nm)	PA excitation (nm)	ε or σ [b]	η [c]	PA enh. [d]	Injected concentration	A/M [e]	Toxicity [f]	Application	Ref.
Gold nanoparticles	Lipoic acid-derived citraconic anhydride	10	650	680	10^7–10^9 cm^{-1} M^{-1} [236]	—	5.7×	30 nM	A	—	Tumor contrast	76
	Poly-di(carboxylatophenoxy) phosphazene (PCPP)	200	>650	700		—	—	75 μg Au	M	Non-significant	Tissue contrast	74
	Diazirine	49	700–900	405 and 808		78.8%	4×	2 mg mL^{-1}	A	None up to 200 μg mL^{-1}	Tumor theranostics	186
	PEO-*b*-PCL	26	800	808		37%	10×	400 μg mL^{-1}	A	Photothermal		75
	Ag shell	84	756	750		—	32×	15 mg kg^{-1}	M	—	Vascular imaging	116
	SiO_2-Gd^{3+}	120	550	532		—	73%	50–1100 pM	M	—	Triple-modality imaging	185
Gold nanocages	PEG	50	825	764–824	0.036 μm^2	—	80%	—	—	—	Cerebral cortex imaging	106
		90	680–1000	700	—	—	5.5×	0.6 pmol	—	—	Tissue contrast	192
	PVP	50	750	735	—	—	3.5×	2 nM	—	—	Sentinel lymph node imaging	111
	PEG-MSH melanocite stimulating hormone	46	778	570 and 778	1.7×10^{-14} m^2	—	36%	10 nM	—	—	Tumor contrast	194
Gold nanoprism	PEG-RGD	110	980 and 530	710	—	—	—	1 mg mL^{-1}	M	None up to 200 μg mL^{-1}	Tumor theranostics	195
	PEG-glucose	94	845	—	—	—	—		—	Photothermal		196
	PEG	110	796–911	800	—	—	—	200 μg mL^{-1}	—	Non-significant		105
		120	830 and 530	710	—	—	—	744 μg mL^{-1}	—		Tumor contrast	103
	SiO_2	120	—	1064	—	—	—	—	—		Sentinel lymph node imaging	104
Gold nanorods	PEG	40 × 12	756	—	10^9–10^{10} cm^{-1} M^{-1} [237]	—	2.3×	5.2 nM	M	Non-significant	Tumor contrast	187
	Gd_2O_2S	70 × 40	820	—		22.6%	3×	50 μg mL^{-1}	M		Tumor theranostics	188
	Poly(*N*-isopropylacrylamide-*co*-methacrylic acid) (PNIPAAmMA)	60 × 10	858	800		—	2×	5 mg kg^{-1}	M	Photothermal		85
	Reduced graphene-oxide	110	750	700 and 800		—	40×	2.5 nM	—	—	Tumor contrast	231
	Melanin	150	600–700	764		—	—	12 mg mL^{-1}	—	None up to 2.75 mg mL^{-1}	Tissue contrast	77
	PEI-microRNA	100	815 nm	—		—	—	0.8 mg mL^{-1}	M	Photothermal	Tumor theranostics	190
	SiO_2	70 × 30	729 nm	720–740		—	—	30 pM	—	—	Stem cells tracking	93
	PEG-Alkyne in PLGA-*b*-PEG	375	680 nm	690		—	10×	110 μM	M	Hemocompatible	Triple-modality imaging	234
Gold nanoshells	PLGA-*b*-PEG-folic acid	165	850–900	860	—	—	—	0.7 mg kg^{-1}	M	Non-significant	Tumor contrast	191
	PEG-antibody	40	710	710	—	—	—	—	—			98
Gold nanostars	PEG-antibody	12	635	720	—	—	4.7×	0.867 mg Au mL^{-1}	—	Photothermal	Tumor theranostics	198
Gold nanotripods	PEG-integrins	<20	700	670	2.02×10^{-16} m^2	—	3×	0.3–12.5 nM	M	Photothermal	Tumor contrast	197

[a] Determined by TEM or DLS. It may refer to the measured hydrodynamic diameter. [b] Measured molar extinction coefficient (ε) or absorption cross-section (σ). [c] Photoacoustic efficiency. [d] Enhancement of the PA signal due to the contrast agent compared to the background or control sample. [e] Activatable (A) or multimodal (M) probes. [f] Collects the evaluations on particle toxicity, if evaluated by the authors.

Table 2 Summary of the physical–chemical properties of nanostructures of other metals and rare earths, together with quantum dots, as *in vivo* PA contrast agents in the recent literature

	Targeting/ coating	Size [a] (nm)	Absorption (nm)	PA excitation (nm)	ε or σ [b]	η [c]	PA enh. [d]	Injected concentration	A/M [e]	Toxicity [f]	Application	Ref.
Pt–Cu alloy NPs	PVP	100	Broad	808	—	—	—	1.34 mg kg^{-1}	M	300 μM	Tumor contrast	207
Bi nanoparticles	PEG-Gd^{3+}	46	700–900	680–900	—	—	—	10 mg mL^{-1}	M	Non-significant	Tumor theranostics	134
Cu nanoparticles	Neodecanoate	80	603 and 746	720–870	—	—	3×	16.99 mg mL^{-1}	—	Previously reported	Sentinel lymph node imaging	206
Co_9Se_8 nanoplates	PAA	100	broad	808	—	—	—	—	M	120 μg mL^{-1}	Tumor contrast	204
$MnMoO_x$ nanorods	C_{18}-PEG	10 × 40	830	830	—	—	2×	5 mg kg^{-1}	M + A	—	Tumor theranostics	205
Pd@Au nanoplates	PEG	30	700	700		28.6%	2.5×	1 mg mL^{-1}	M	—	Tumor contrast	209
Pd nanosheets	PVP	16	790	790	—	—	3.4×	0.8 mg mL^{-1}	—	—	Tumor contrast	129
Silver nanoplates	PEG	25–220	550–1080	740–940	—	—	—	10^{12} nanoplates in 200 μL	—	None up to 1 mg mL^{-1}	Tumor contrast	210
Silver bumpy nanoprobes	SiO_2-BSA	200	680	680–950	—	—	70%	20 μM	M	—	Sentinel lymph node imaging	211
TiS_2 nanosheets	PEG	100	800	808	26.8 L g^{-1} cm^{-1}	—	4×	2 mg mL^{-1}	—	—	Tumor contrast	131
Titanium nitride NPs	PEG	20	600–1000	808	28.6 L g^{-1} cm^{-1}	48%	1.3×	2 mg mL^{-1}	M	—	Tumor contrast	212
WS_2 nanosheets	PEG	50–100	700–1000	700	23.8 L g^{-1} cm^{-1}	—	6×	5 mg mL^{-1}	M	—	Tumor theranostics	132
Upconversion NPs	α-Cyclodextrins	29	—	980	—	—	—	0.5 mg mL^{-1}	—	None up to 0.2 mg mL^{-1}	Tissue contrast	199
Bi_2Se_3 nanoplates	PVP	70	broad	1064	—	—	19.6×	15.26 mg mL^{-1}	—	None up to 1 mg mL^{-1}	Tissue contrast	208
Black phosphorus QDs	$Ti(OTs)_4$	2	680	680	22.2 L g^{-1} cm^{-1}	—	6×	200 μg in 100 μL	—	Non-significant	Tumor contrast	201
	PEG	22	808	680	2.1 L g^{-1} cm^{-1}	—	—	2 mg mL^{-1}	—	Photothermal	Tumor theranostics	202
Uranium	PLGA	335	848	910	—	—	1.8–7.4×	0.38 nM (2.75 mg mL^{-1})	—	—	Tissue contrast	133
CuS nanoparticles	PEG	11	990	1064	2.6×10^7 cm^{-1} M^{-1}	—	—	6–96 μg mL^{-1}		None up to 96 μg mL^{-1}	Deep tissue imaging	128
	Citrate	20	680 and 930	680 and 930	—	—	—	0.8 mg mL^{-1}	A	Non-significant	Tumor contrast	123
$Cu_{2-x}Se$ nanocrystals	DSPE-PEG	7.6	1150	900	2×10^{-18} m^2	—	4.8×	800 nM	—	IC_{50} = 22.5 pmol mL^{-1}	Sentinel lymph node imaging	125
CuInS/ZnS	DSPE-PEG	25 and 80	650–750	—	—	11.6%	—	2 mg mL^{-1}	M	Non-significant	Tumor theranostics	203
$Cu_{2-x}S$ nanodots	DSPE-PEG	12	1064	1064	—	—	410×	10 mg Cu per kg	—	None up to 100 ppm	Tumor theranostics	122

[a] Determined by TEM or DLS. It may refer to the measured hydrodynamic diameter. [b] Molar extinction coefficient (ε) or absorption cross-section (σ) measured for the nanosystem. [c] Photoacoustic efficiency. [d] Enhancement of the PA signal due to the contrast agent compared to the background or control sample. [e] Activatable (A) or multimodal (M) probes. [f] Collects the evaluations on particle toxicity, if evaluated by the authors.

Table 3 Summary of the physical–chemical properties of carbon and polymeric nanostructures as *in vivo* PA contrast agents in the recent literature

	Targeting/coating	Size [a] (nm)	Absorption (nm)	PA excitation (nm)	ε or σ [b]	η [c]	PA enh. [d]	Injected concentration	A/M [e]	Toxicity [f]	Application	Ref.
Carbon nanotubes	Pluronic	2	Broad	740–820	5×10^3 M^{-1} cm^{-1}	—	5×	0.5 mg mL^{-1}	M	—	Sentinel lymph node imaging	140
	PEG	80–100	Broad	808	(ref. 238)	—	5×	2 mg mL^{-1}	—	Non-significant	Tumor contrast	217
	PEG-RGD	50–300	Broad	710–780		—	80%	50 nM	—	Non-significant	Tissue contrast	216
Graphene	BSA	70	Broad	808 nm	—	—	55%	1 mg mL^{-1}	—	Non-significant	Tumor contrast	146
Fullerenes on SiO_2	PHF	50–100	Broad	785 nm	—	—	100%	0.45 mg mL^{-1}	—	Non-significant	Tumor contrast	218
Carbon nanoparticles	Citric acid-antibody	12	425	680–760	—	—	—	7 mg mL^{-1}	—	Photothermal	Tumor theranostics	220
	—	70	820	820	—	—	9.2×	90.3 μg mL^{-1}, 0.238 nM	—	Non-significant	Tissue contrast	221
	PEG	7	510	510	—	—	60%	25% vol. 100 μL	—	Non-significant	Sentinel lymph node imaging	219
Polypyrrole NPs	PEG-Gd^{3+}	70	Broad	—	—	—	3×	5 mg mL^{-1}	M	Photothermal	Tumor theranostics	163
	PVA	46	Broad	808	2.4×10^{10} cm^{-1} M^{-1}	—	—	2 mg mL^{-1}	—	Non-significant	Vascular imaging	161
Polythiophenes	1,2-Dipalmitoyl-*sn*-glycero-3-phosphocholine (DPPC)	40	660–700	700–820	5.0×10^7 cm^{-1} M^{-1}	—	13.3×	50 μg	M	Non-significant	ROS imaging	222
		120–160	700–825	600–1000	250 cm^{-1} L g^{-1}	—	[–1]	1.6 μg in 10 μL	—	Non-significant	Vascular imaging	162
	DSPE-PEG-folate	50	700–850	700–900	—	—	4×	0.3 mg mL^{-1}	—	—	Tumor contrast	160
	PEG-phospholipid-Gd^{3+}	110	670	680	—	—	3.5×	0.1 mg mL^{-1}	M	Photothermal	Tumor theranostics	157
	PEG-*b*-PPG-*b*-PEG	55	840	750	—	—	2.6×	0.1 mg mL^{-1}	—	Photothermal	Tumor theranostics	158
	DSPE-PEG	50	710	800	—	—	5.5×	0.5 mg mL^{-1}	—	Non-significant	Sentinel lymph node imaging	166
Diketopyrrolopyrrole-based	PEG-*b*-PPG-*b*-PEG	11–54	744–253	750–1064	—	—	1.5×	6 mg mL^{-1}	—	None up to 0.5 mg mL^{-1}	Tissue contrast	226
	DSPE-PEG	68	809	1000–1200	—	—	3.4×	50 μg mL^{-1}	M	None up to 150 μg mL^{-1}	Tumor contrast	171
	PEG-*b*-PPG-*b*-PEG	40	616–665	680	—	—	4.7×	30 μg in 120 μL	—	Non-significant	Tumor contrast	164
	SiO_2-PEG	18	680–860	680	—	—	1.5×	0.1 mg mL^{-1}	—	—	Protein sulfenic acid imaging	225
	DSPE-PEG	45	748	710–850	76 mL $(mg\ cm)^{-1}$	—	5.3×	30 μg in 120 μL	—	Non-significant	Tumor contrast	213

[a] Determined by TEM or DLS. It may refer to the measured hydrodynamic diameter. [b] Molar extinction coefficient (ε) or absorption cross-section (σ) measured for the nanosystem. [c] Photoacoustic efficiency. [d] Enhancement of the PA signal due to the contrast agent compared to background or control sample. [e] Activatable (A) or Multimodal (M) probes. [f] Collects the evaluations on particle toxicity, if evaluated by the authors.

humans.[181] Study participants have been subcutaneously injected with MB in the same breast area as their primary breast cancer. Patients underwent noninvasive PA imaging at the injection site. To correctly differentiate the contrast from the surrounding vessels, PA images have been acquired at two different wavelengths (650 and 1064 nm) and compared, obtaining signal enhancement factors of 1.75 on SLNs in the tumor region. As has already been said, SMDs suffer from some important drawbacks, which drastically limit the employability of molecular contrast agents in their free form. These are (1) fast clearance from the circulatory system due to the immune response of the organism, (2) concentration-dependent optical behavior, caused by intrinsic lipophilicity of polyconjugated chromophores, (3) small optical absorption wavelength and low extinction coefficients. Because of this, the attention of scientific research has been directed towards the employment of specifically engineered nanostructured contrast agents, which can overcome the intrinsic limitations of SMDs.

It is worth reporting that the possibility of exploiting different phenomena for the generation of photoacoustic signals upon laser exposure has been lately explored. In particular, in 2012, Wilson *et al.* proposed that laser-induced vaporization of perfluorocarbon nanodroplets could induce PA contrast in biological systems.[182] Even though this could provide efficient PA contrast *in vivo*, the system requires the employment of small molecule dyes as photoabsorbers, with all the limitations associated with dye-based PA contrast.

Metal and semiconducting nanoparticles

Gold. Due to their small size, gold nanoparticles have LSPR bands in the visible, up to 600 nm. To adapt them for PA imaging *in vivo*, AuNPs need to form stable aggregates to red-shift their plasmon band.[183,184] Otherwise, the PA penetration depth for short wavelengths limits their application to superficial targets such as rat brains. In 2012, Kircher *et al.* presented a Magnetic–Photoacoustic–Raman (MPR) triple modality imaging nanoparticle for brain tumor imaging, both *in vitro* and in living mice.[185] Their probe was built as a gold-core silica-shell SERS nanoparticle decorated with paramagnetic Gd^{3+} ions, allowing for picomolar sensitivity of MRI, PA imaging and SERS imaging of glioblastoma *in vivo* (Fig. 9). Since the nanoconstruct displayed its optical absorption maximum at 550 nm due to its spherical gold core, the authors implemented a 525 nm laser in their home-made PA imaging setup. In particular, they obtained significant PA contrast at concentrations as low as 1.22 pM in phantoms, and they observed a 75% increase of the photoacoustic signal of the tumor after tail vein injection of MPRs in tumor-bearing mice. No accumulation was observed in the healthy tissues, allowing for the identification of tumor borders to facilitate resection.

Lately, Cheng *et al.* reported the fabrication of a light-triggered assembly of gold nanoparticles which could serve as a contrast agent for PA imaging of tumors.[186] The nanoparticles described were composed of a 20 nm gold core functionalized

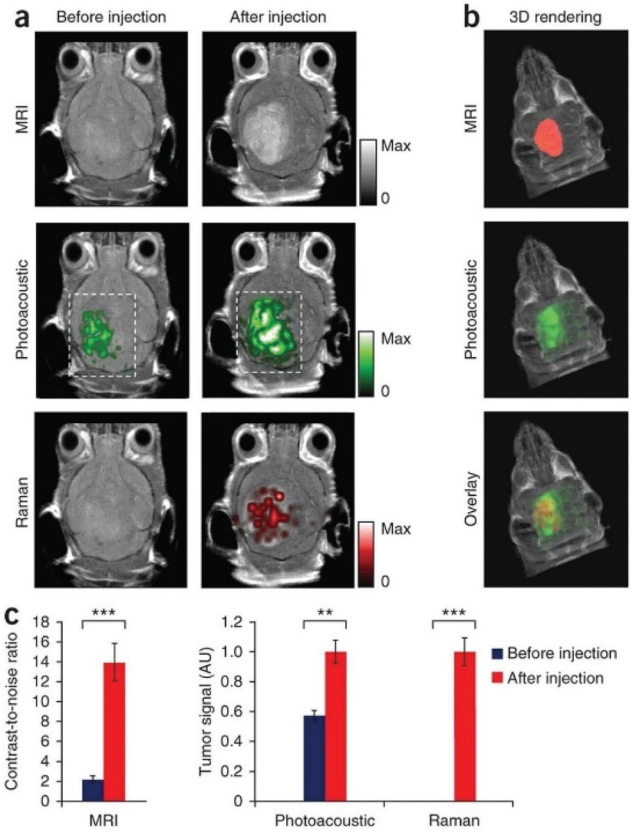

Fig. 9 *In vivo* triple modality imaging of MPR nanoparticles. (a) MRI, PA and Raman 2D axial images before and after injection of MPRs, (b) 3D rendering of MRI and PA signals, and their overlay, showing good tumor contrast, (c) quantification of MRI, PA and Raman signal intensity before and after the injection of the nanoconstruct. Notwithstanding the limitations in PA imaging penetration depth due to the short excitation wavelength employed, thanks to glioblastoma superficiality strong PA contrast has been obtained; adapted from ref. 185.

with diazirine moieties on covalently-linked PEG chains. Upon irradiation with 405 nm laser light, diazirine groups cross-link, leading to covalent aggregation. The surface plasmon bands of gold cores shift to the NIR, leading to aggregates with photoacoustic efficiency as high as 78.8%, with negligible cytotoxicity to 4T1 cells up to 200 μg mL^{-1}. After the assessment of the feasibility of laser-induced aggregation *in vivo*, the authors injected 100 μL of 2 mg mL^{-1} of AuNPs in the tail vein of female nude mice bearing 4T1 tumors. Tumors have been exposed to 405 nm laser light for 25 s to induce aggregation at the tumor site, followed by PA imaging. Compared to control animals, images obtained from tumor-bearing mice showed increased PA contrast at the tumor site.

Recently, gold nanorods have found various applications on the basis of their photoacoustic response to exploit them for tumor detection *in vivo*. In 2012, Jokerst *et al.* exploited localized surface plasmon for SERS (surface-enhanced Raman scattering) on the GNR surface: dual-modality SERS and PA gold nanorods have been used to image subcutaneous ovarian tumor xenograft models (OvCA) *in vivo*,

showing how GNRs could offer both photoacoustic signals for diagnostics and tumor visualization and optical SERS for image-guided resection.[187] For this purpose, GNRs have been prepared with the absorption band in the NIR for PA signals and then functionalized with an IR laser dye and thiol-PEG to ensure an intense SERS response. By means of their photoacoustic response, intravenously injected GNRs have been shown to accumulate by the EPR effect in 2008, HEY and SKOV3 OvCA tumor cells, allowing for efficient tumor visualization. On the other hand, SERS has been exploited for tumor edge identification and for image-guided resection on tumor xenografts from the 2008 cell line OvCA model.

Guo *et al.* recently reported the preparation of gadolinium oxysulphide-coated gold nanorods as dual-modality contrast agents for PAI and MRI, employing the strong MRI contrast of gadolinium, which is strongly paramagnetic due to its seven unpaired electrons.[188] GNRs have been prepared with the previously described seeded-growth method, and coating with gadolinium oxysulphide has been performed *via* a one-step process with Gd nitrate as a gadolinium source in the presence of ascorbic acid (AA) and thioacetamide (TAA) at 80 °C. Then, NPs have been further modified with polyvinyl alcohol (PVA) for stabilization. Increasing the Gd_2O_2S shell thickness could increase the effective dielectric constant surrounding the plasmonic core, resulting in a red-shift of the longitudinal LSPR mode. The PA and MRI response of the nanosystem has been tested both *in vitro* and *in vivo*. Once the feasibility of the study was proved, GNRs@Gd_2O_2S has been intratumorally injected into Hep G2 tumor-bearing BALB/c nude mice as a model for *in vivo* PAI/MRI dual-modal imaging. A 4-fold increase in PA signal and a 2-fold increase in MRI contrast have been observed after injection, demonstrating the effect of the system as a dual-modality contrast agent.

An additional interesting application of GNRs in photoacoustic imaging has been described by Du *et al.*[189] The authors demonstrated the possibility of building a nanoplatform by assembling GNRs on the surface of a DNA-origami nanostructure. The nanostructured hybrid, which combines the well-known optical properties of GNRs with the enhanced passive tumor targeting and long-lasting effects of DNA nanostructures, has been exploited as a unique probe and an efficient contrast agent in PAI, generating intense signals at very low concentrations. PAI has been performed on breast-tumor xenografted mice in which DNA-GNRs nanoplatforms have been intravenously injected, revealing enhanced tumor accumulation compared to bare GNRs. Accumulation of gold *via* EPR effect has been observed to be slower but more persistent with DNA-GNRs compared to bare GNRs, giving rise to elevated tumor/muscle contrast ratio even 24 h post-injection (Fig. 10).

In 2018, Chen and co-workers developed polyethyleneimine-modified GNRs (GNRs-PEI) connected to a Fuel Improved microRNA Explorer (FIRE) capable of distinguishing tumor cells from healthy tissues efficiently.[190] Their nanoconstruct was able of carry out active targeting, thanks to the detection of microRNA-21 strands, upregulated in cancer cells, by designing a smart fluorescence quenching approach in which the fluorescence signal was expected to be much stronger for tumor tissues than for the healthy one. Their platform demonstrated good tumor inhibition efficacy *in vivo via* both

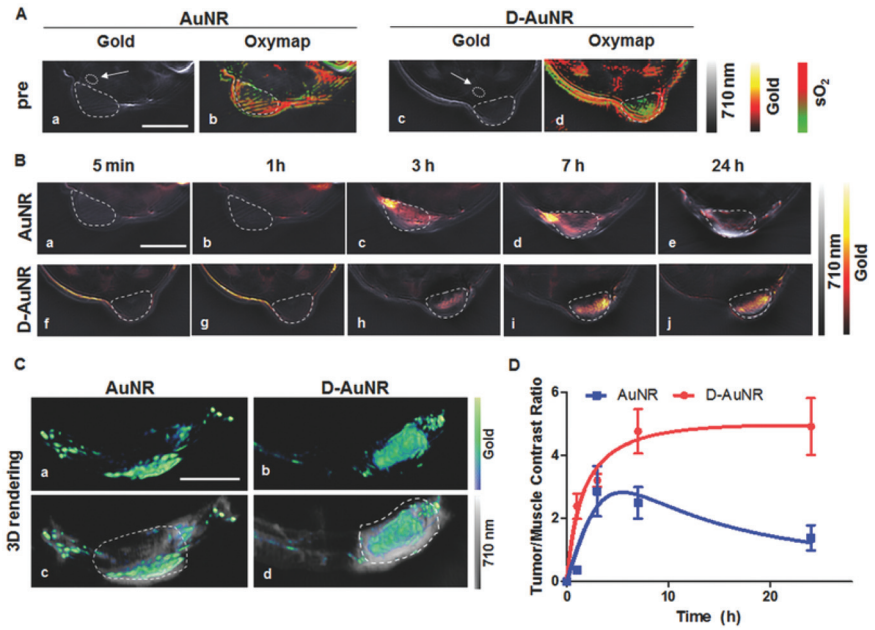

Fig. 10 (a) Gold distribution and the corresponding oxygen saturation maps before intravenous injections of GNRs and GNRs-DNA in 4T1-tumor-bearing mice. (b) GNRs and DNA-GNRs distribution after intravenous injection, (c) 3D rendering of the tumor region 24 h post-injection and (d) PA contrast ratio between tumor and muscle for GNRs and DNA-GNRs as a function of time after the injection. Adapted from ref. 189.

fluorescence imaging and photoacoustic imaging-guided photothermal therapy. To evaluate PA contrast, 100 μL of 0.8 mg mL^{-1} GNRs-PEI solution have been intratumorally injected into tumor-bearing mice, revealing strong PA signals that can be easily differentiated from the background at the tumor site.

Recently, we described the fabrication of a core–shell composite nanomaterial in which a paramagnetic Fe_3O_4 core has been covered with a layer of silica on which a gold shell has been grown.[191] The so-called Fe_3O_4@SiO_2@Au NPs have been entrapped in polymeric micelles to protect the metallic core from the biological environment; then they have been further conjugated to folic acid to ensure specific targeting to IGROV ovarian cancer cells. The nanoconstruct, which displayed a hydrodynamic radius of about 165 nm, had its optical absorption maximum between 850 and 900 nm with a high molar absorption coefficient and no fluorescence properties; this made the core–shell system a good candidate for the multispectral PA imaging of tumor models *in vivo*. Xenograft tumor-bearing mice were systemically injected with folic acid-conjugated Fe_3O_4@SiO_2@Au NPs at concentrations of 8 mg Au per kg, and the tumor was imaged at 860 nm 4 h post-injection for maximum sensitivity. The magnetic core allowed for MRI, making the core–shell system a sensitive dual-modality imaging platform for the detection of ovarian cancer.

As previously introduced, gold nanocages can represent powerful theranostic platforms, and they can give rise to high PA signals, thanks to their surface plasmon features. In 2014, Jeon *et al.* described the use of NIR-absorbing gold nanocages to image the murine bladder *in vivo*.[192] PEGylated gold nanocages (λ = 700 nm) have been prepared by galvanic replacement reaction on silver nanocubes and covalently linked to PEG-SH for biocompatibilization. After transurethral injection of a 2 nM solution of nanocages, rats underwent non-invasive PA cystography and displayed a 22.4× enhancement of PA signal compared to the control sample. Moreover, no more signal could be observed in the bladder after 24 h, suggesting that the injected nanosystem was not retained in the bladder but washed away by the urine.

Sakthi Kumar and co-workers recently described the production of gold nanocages for the first contrast-based PA imaging of the eye.[193] The nanosystem was produced by an ultrafast microwave-assisted procedure, which led to nanocages with a uniform edge size of about 50 nm, showing strong optical absorption properties at 900 nm. After the evaluation of the PA contrast potential in polyethylene tubes for the obtained nanostructure, nanocages have been injected right above the iris of an enucleated porcine eye, showing a PA contrast enhancement of 50% and thus leaving the open possibility of surface modification of nanocages to enable active targeting for specific eye diseases (Fig. 11).

Kim *et al.* have reported the applications of gold nanocages for molecular PA imaging of melanomas.[194] Nanocubes, prepared by the traditional galvanic replacement method, have been conjugated with [Nle4,D-Phe7]-α-melanocyte-stimulating hormone in order to bind to α-MSH receptors overexpressed in

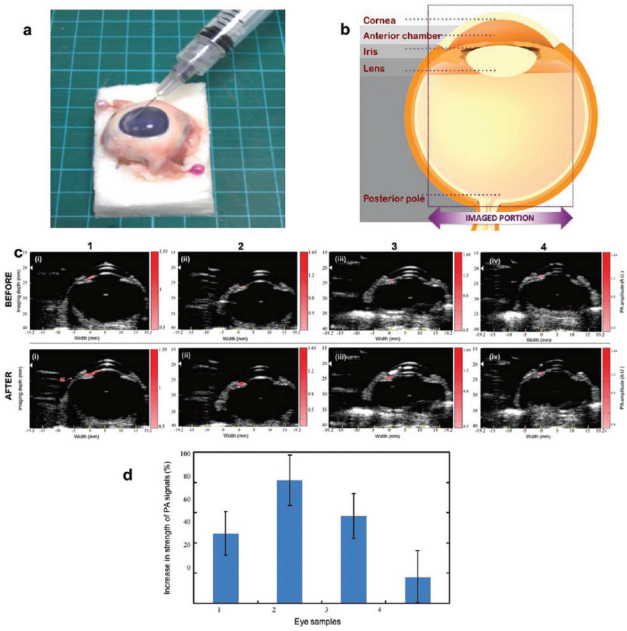

Fig. 11 (a) Photograph of the enucleated porcine eye. (b) Schematic representation of the eye parts. (c) PA images acquired before and after the injection of nanocages in four different eye samples, showing increased PA contrast. (d) PA contrast enhancement for the four injected samples. Adapted from ref. 193.

melanomas. The authors injected 100 μL of 10 nM targeted Au nanocages into the tail vein of mice; 6 h later, the mice underwent PA imaging at the tumor site with a 778 nm pulsed laser. They observed 300% PA signal enhancement at the tumor site compared to the signal in mice injected with the same amount of untargeted nanocubes, showing both the efficacy of their active targeting system and the efficiency of gold nanocubes for PA contrast. In addition, PA has been employed to image the vasculature surrounding the tumor, obtaining more information about the melanoma state. This has been performed by tissue laser excitation at 570 nm.

In 2016, Bao *et al.* have shown, in their work, how peptide-conjugated gold nanoprisms (AuNPrs) could serve as a PA contrast agent for tumor angiography and *in situ* imaging of a murine orthotopic gastric carcinoma model.[195] By scanning the tumor site with a PA setup at 710 nm, the tumor vasculature has been visualized before and 1, 3 and 6 h after tail-vein injection of peptide-coated PEGylated AuNPrs at 1 mg mL^{-1} concentration, showing retention of good contrast at the tumor site. In parallel, antibody-conjugated AuNPrs have been used to image gastric cancer by photoacoustic detection of the accumulation of the gold nanostructure. Since most PA photoabsorbers have potential application in photothermal therapy (PTT), AuNPrs have been exploited to directly measure by PA imaging the reduction in tumor size after prolonged exposure to continuous 980 nm laser light. Their results clearly showed triangular gold nanoprisms as two molecular probes with high sensitivity contrasts and therapeutic agents for tumor detection *in vivo*, which represent a safe theranostic nanoplatform

as confirmed by the histological analysis performed on organ tissues after 14 days from the injection.

The same year, Han *et al.* described the fabrication of glucose-functionalized gold nanoprisms with improved cellular uptake and cytotoxicity in cancer cells.[196] In comparison with target-less nanoparticles, glucose conjugation helped towards the accumulation of photoabsorbing AuNPrs in cancer cells. The authors injected 100 μg of 1 mg mL^{-1} of glucose-conjugated PEGylated nanoprisms into MGC-803 cell tumor-bearing nude mice. PA imaging of the tumor showed great contrast enhancement, increasing with time post-injection by excitation at 778 nm. A weaker tumor profile was observed after the injection of untargeted PEGylayed nanoprisms, compared to the control image obtained after the injection of PBS solution. The authors explored whether their nanoconstruct could serve as a photothermal therapy agent, showing remarkable results and drastic tumor growth inhibition.

Cheng *et al.* firstly reported in 2014 the production of 20 nm gold nanotripods as a contrast agent for *in vivo* photoacoustic imaging.[197] Gold nanotripods displayed cross-sections of the order of 10^{-18} m^{-2} at 700 nm, generating 33% more contrast than the same mass of gold nanorods. As a proof-of-concept, the authors conjugated cyclic Arg-Gly-Asp-D-Phe-Cys (RGDfC) peptide to PEGylated nanotripods to demonstrate the effective contrast *in vivo* by active targeting. PA imaging has been performed at 700 nm on living mice after the injection of 100–200 μL of targeted gold nanotripods in PBS, 0.5 to 4 h post-injection. Compared to control experiments, the nanostructure could provide more than 3 times higher PA contrast. Moreover, the signal intensity has been observed to respond linearly to variations of the injected concentration (Fig. 12). Intravenous injection of nanotripods displayed increased contrast at subnanomolar, generating images that well correlated with the corresponding PET studies.

Liang *et al.* reported in 2015 the preparation of highly branched gold nanoparticles named gold nanostars (GNSs) displaying strong PA contrast.[198] The nanostructure displayed an absorption maximum at about 635 nm and the hydrodynamic radius has been measured to be around 100 nm. Due to their promising properties, anti-CD44 and anti-CD44v6 monoclonal antibodies have been conjugated to PEGylated nanostars, to evaluate the interaction between the nanoprobes and gastric cancer stem cells (GCSCs). To evaluate PA contrast *in vivo*, the authors intravenously injected 150 μL of gold 0.867 mg mL^{-1} as conjugated gold nanostars, and monitored the PA signal intensity at the tumor site over time. Results showed a contrast enhancement by a factor 4.7 and 2.5 for nanostars targeted with CD44v6 and CD44, while only a factor of 1.75 was observed after the injection of untargeted GNSs, showing the reliability of both the contrast from nanostars and the effectiveness of the active targeting.

In summary, gold nanostructures can be considered as some of the most promising nanostructured contrast agents for PA imaging, offering wide shape- and size-dependent absorption behaviour, high photoacoustic conversion efficiencies and well known biocompatibility. They also show high extinction coefficients thanks to the localized surface plasmon resonance (LSPR) phenomena, which allows the employment of low injected concentrations to achieve efficient contrast *in vivo*. Moreover, since their surface chemistry is well known and deeply explored in the literature, gold nanostructures can be easily functionalized either with active targeting agents or with additional functional probes, which allows their employment for tumor imaging in multiple modalities, such as MRI,

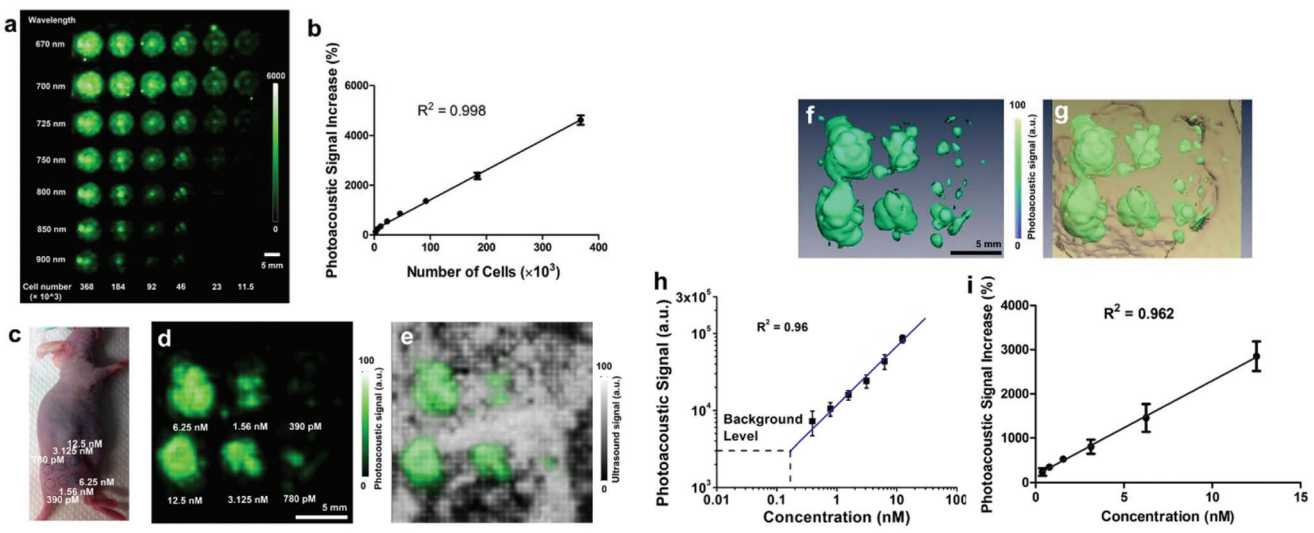

Fig. 12 (a) PA images of agar phantoms containing U87MG cancer cells exposed to RGD-conjugated gold nanotripods at different cell concentrations and for different excitation wavelengths. (b) Linear correlation between photoacoustic signal and the number of treated cells in the phantom. (c) Optical picture of a treated mouse, with injection sites highlighted by the injected concentration. (d, e) PA imaging of the area subcutaneously injected with the nanoconstruct, showing the different injection sites with different intensities. (f, g) 3D volume rendering of PA (green) and US (brown) signals recorded. (h, i) Linear correlation between the injected concentration and photoacoustic signal *in vivo*. Adapted from ref. 197.

CT, PET, SERS and optical imaging. Amongst other gold nanostructures, the most promising results have been obtained with gold nanorods (GNRs): their longitudinal LSPR can be finely tuned in the synthesis step throughout the NIR, allowing us to specifically design GNRs to overcome the different endogenous contrast in different biological tissues.

Quantum dots and rare-earths

Upconversion nanoparticles (UCNPs) are Yb^{3+} and Er^{3+} co-doped $NaYF_4$, which are characterized by efficient NIR-to-visible optical conversion, thanks to energy transfer processes between Yb and Er. In 2014, Maji *et al.* described how luminescence from UCNPs could be quenched to ensure high PA contrast *in vivo* upon irradiation at 980 nm.[199] Lipophilic UCNPs displayed the characteristic emission bands from Er^{3+}. By encapsulating the doped nanoparticles in α-cyclodextrins, hydrophilic UCNPs (UC-α-CD) have been obtained. Hence, the quenching effect of water as a solvent strongly reduced the luminescence of the particles in favour of a remarkable PA contrast enhancement. PA images have been acquired before and 35 min after the intravenous injection of 250 μL of UC-α-CD at 500 μg mL^{-1} concentration. Results showed signal retention enhancement at the kidney while the cytotoxicity tests revealed the non-toxicity of the nanostructure up to 200 μg mL^{-1}, supporting the applicability of rare-earth doped semiconducting nanoparticles in photoacoustic imaging by effective water quenching.

The same year, Sheng *et al.* reported the synthesis of rare-earth doped $NaYF_4$ with different morphologies for similar applications.[200] These authors intravenously injected NaYF4:Er,Yb with different surface stabilizers in living mice, declaring a signal enhancement of 2.7 times the background by excitation at 975 nm.

Lately, Sun *et al.* described how TiL_4-coordinated black phosphorus (TiL_4@BP) quantum dots could serve as a contrast agent for *in vivo* PAI of cancer, as an improvement of a previous study from 2016.[201,202] The QDs' average size was 2.8 nm, and they displayed molar extinction coefficients of 22.2 L g^{-1} cm^{-1} at 680 nm, 3.6 times higher than the one measured for GNRs when compared on a per mass basis. To evaluate the effective PA contrast that could be generated *in vivo*, 200 μg of TiL_4@BP QDs have been intravenously injected into eight MCF-7 tumor-bearing Balb/C nude male mice. PA images have been obtained by summing the PA response acquired from five laser pulses at 608 nm in 15 nm steps before and 0.5 to 48 h post-injection. The obtained images demonstrated the effective accumulation of TiL4@BP QDs in the tumor, with a maximum contrast obtained 4 h post-injection and still weakly retained after 48 h from the administration. No relevant cytotoxicity has been detected *in vitro*.

Lv and coworkers reported in 2016 the NIR-emission properties of CuInS/ZnS (ZCIS) QDs for both tumor fluorescence and photoacoustic imaging.[203] The authors prepared two similar nanosystems with different sizes (25 and 80 nm) to evaluate differences in the diffusion profiles and tumor uptake. The QDs displayed strong optical absorption at 650–750 nm, suggesting a potential PA imaging ability. Multispectral Optoacoustic (MSOT) imaging was performed between 680 and 900 nm at different time steps after the intravenous administration of 200 μL of 2 mg mL^{-1} ZCIS solution in nude mice bearing 4T1 tumors. The experiments revealed size-dependent particle accumulation and cleavage at the tumor site: smaller particles have longer tumor retention times and tumor uptake compared to the bigger ones (Fig. 13).

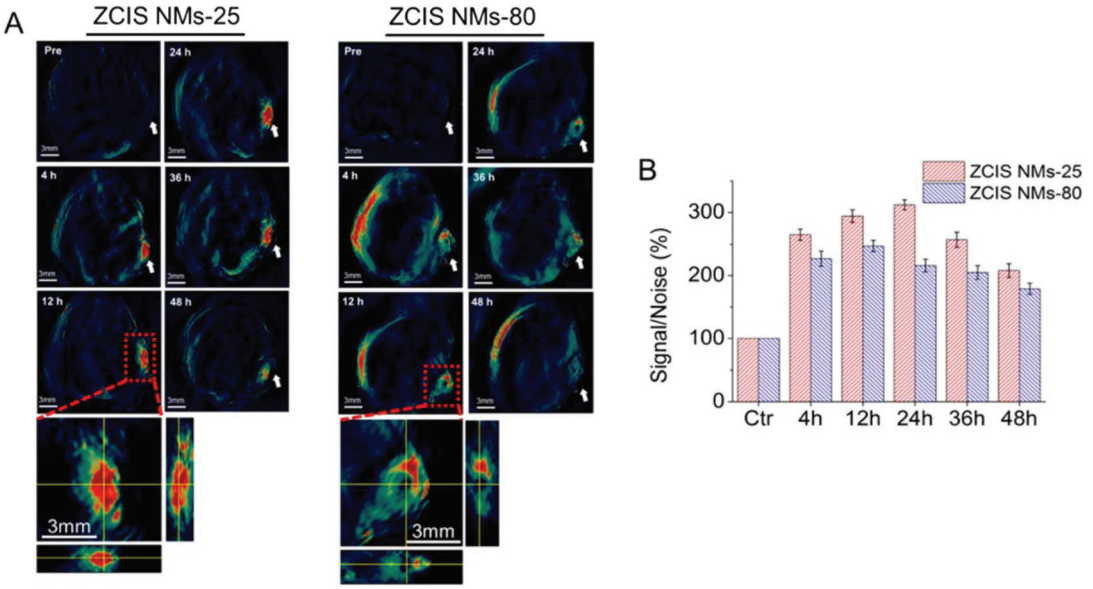

Fig. 13 (A) *In vivo* MSOT imaging of 4T1 tumor-bearing nude mice injected with ZCIS of 25 nm (NMs-25) or 80 nm (NMs-80) at different time steps after the injection, revealing higher contrast at the tumor site for smaller particles. (B) Average MSOT signal intensity at the different time steps. Adapted from ref. 202.

In addition, fluorescence from the QDs allowed for fluorescence imaging, which confirmed the results from PA imaging. Furthermore, the ability of ZCIS to mediate photoinduced tumor ablation was evaluated with success.

To sum up, nanosystems containing or composed of this exotic class of materials display good photoacoustic contrast and most of them can be also employed for fluorescence imaging due to their widely reported photoemission behaviour. There are still few examples of their application in PA imaging; great effort still needs to be directed towards the study of their bioaccumulation and toxicity; notwithstanding their excellent and tunable photophysical properties, quantum dots and rare-earth nanoparticles still suffer from poor biocompatibility and high production costs which, nowadays, drastically limit the potential translation of this class of nanosystems into the clinics.

Other metals. In 2015, Song and co-workers presented a paper on Co_9Se_8 nanoplates for PA/MRI dual-modality imaging and photothermal therapy (PTT).[204] Poly(acrylic acid) functionalized cobalt chalcogenide nanoparticles (PAA-Co_9Se_8 nanoplates) are reported to display strong NIR absorption properties and increased biocompatibility. Also, due to cobalt paramagnetism, the nanoconstruct could efficiently serve as a MRI contrast agent. The large surface area of nanoplates allowed for increased drug loading, tested with doxorubicin (DOX) as a proof-of-concept. PA imaging was performed with an 808 nm pulsed laser after the injection of PAA-Co_9Se_8 nanoplates into HepG2 liver tumor-bearing mice, showing a strong photoacoustic response around the tumor region, while only major vessels could be identified before the injection. MRI images displayed clear contrast enhancement at the tumor site after injection, as in PA imaging. Moreover, positive results have been obtained from the release profiles of loaded DOX and a drastic reduction in tumor growth after photothermal treatment of nanoplate-injected mice. Even though the employment of cobalt in the nanostructure allows for simultaneous PA and MRI of the tumor region, the authors did not evaluate the photothermal behaviour of the nanoplates, making it hard to compare their contrast performances with contrast media of different nature. However, the broad NIR absorption of PAA-Co_9Se_8 nanoplates makes them a versatile contrast agent, allowing us to adapt the PA excitation wavelength to the different biological transparent windows of different biological tissues.

Lately, Gong *et al.* described the production of PEGylated $MnMoO_x$ nanorods as a PA probe for the identification of glutathione (GSH) *in vivo*.[205] GSH is an easily oxidizable tripeptide with good antioxidant properties. Their nanoprobe was capable of actively targeting without the need for any surface modification but exploiting the chemistry of the core elements themselves. In fact, GSH was able to reduce Mo^{VI} to Mo^{V} efficiently, thus causing the disruption of the non-absorbing nanorod and providing contrast from strongly absorbing nanodots. Since GSH is overexpressed in various tumor tissues, their system was able to provide efficient PA contrast *in vivo* at the tumor site by excitation at 830 nm, revealing contrast capability triggered by the tumor itself. Moreover, the release of Mn^{2+} ions during GSH activation allowed for the possibility to employ T_2-weighed MRI to co-detect tumor localization. To further study the potential of the nanosystem for GSH detection, mice bearing 4T1 tumors were intravenously injected with PEGylated $MnMoO_x$, revealing 2× PA signal enhancement at the tumor site compared to healthy muscle tissue. This work reports a smart approach for the generation of tumor-induced PA and MRI contrast, since it is the tumor itself that chemically modifies the small nanorods through the overexpression of GSH. Here, intravenous injection of the nanorod dispersion allows for PA contrast at the tumor site without the need for any active targeting; however, the conjugation of active targeting species such as antibodies, nucleic acids or small targeting molecules could, in principle, increase the specificity of the contrast and reduce the distribution of manganese- and molybdenum-based compounds in the body.

Pan *et al.* have reported the synthesis of copper neodecanoate nanoparticles for PA imaging of SLNs.[206] In their work, the authors for the first time produced a copper-based contrast agent for SLN detection by PA imaging *in vivo*. Their nanoconstruct was an 80 nm wide self-assembled copper neodecanoate nanoparticle encapsulated in phospholipid micelles, which displayed an optical absorption maximum at λ = 603–746 nm. The absorption is believed to originate from crystal field splitting of Cu^{2+}-neodecanoate complexes, and it has been thought to be exploitable for PA imaging. After the administration of 1 mg mL^{-1} nanoparticle suspension in living mice, bright PA contrast was observed immediately and 60 min post-injection. A signal enhancement of 500% has been measured for a 20% colloidal suspension of nanoparticles, much faster accumulation rates compared to GNRs. However, compared to most other reviewed nanostructured contrast agents, copper neodecanoate nanoparticles display a quite blue-shifted absorption (below 800 nm) which can severely limit the PA response of the nanosystem in deep tissues.

In 2016, Zhou *et al.* developed dendritic Pt–Cu alloy nanoparticles (DPCNs) as multimodal imaging and guided chemophotothermal therapy (CTP).[207] Furthermore, they demonstrated that their construct could serve as light and a pH-triggered drug delivery platform, and the promising photothermal properties of DPCNs suggested their implementation for PA imaging and CTP. Thanks to their elevated surface area, dendritic structures can adsorb an increased amount of small molecules, improving their performances in drug loading capacity. Firstly, negligible cytotoxicity was observed up to 300 μM; therefore, tumor-bearing mice were intravenously injected with DPCN at a dose of 1.34 mg kg^{-1} to undergo PA imaging analysis. Imaging results showed efficient nanoparticle accumulation in the tumor and strong contrast enhancement at different time steps after injection (0 to 24 h).

Lately, Park *et al.* reported the novel synthesis of Bi_2Se_3 nanoplates for long-wavelength PA imaging of sentinel lymph nodes *in vivo*.[208] Thanks to their absorption after 1000 nm, and thus the employment of low-energy highly penetrating radiations, PA imaging of deep tissues has been explored. After

the complete evaluation of the photophysical properties of the exotic material, PA imaging contrast has been first evaluated *ex vivo* in deep chicken tissues by excitation at 1064 nm (ND:YAG laser); then it has been employed to image small animals. In parallel, 50 μL of 15.26 mg mL^{-1} nanoplates have been transurethrally administered to Balb/c mice for contrast-based cystography; 200 μL of the same solution has been orally given to mice for the imaging of the gastrointestinal tract and an additional 20 μL have been subcutaneously injected to image sentinel lymph nodes. For all the investigated tissues, strong PA signal enhancement was observed, with high signal-to-noise ratio and reduced cytotoxicity. In this study, the authors reported very strong PA signal enhancement both in the bladder and at the lymph nodes, but it should be noted that the injected concentration is relatively high (over 15 mg mL^{-1}); thus, detailed toxicity and bioaccumulation studies should be performed to evaluate the impact of high concentrations of bismuth and selenium on the health of treated mice.

Chen *et al.* described in 2014 a novel nanostructured theranostic platform based on core–shell Pd@Au nanoplates for *in vivo* PA imaging, CT imaging and PTT.[209] Hexagonal palladium nanosheets with an average diameter of 26 nm were covered with a tunable shell of gold for optical absorption properties in the 600–1300 nm region. To quantify PA contrast from Pd@Au nanoplates, Balb/c mice were injected with 300 μL of 1 mg mL^{-1} PEGylated nanoplate solution and PA images have been recorded at 1 to 24 h post-injection. After prolonged accumulation by the EPR effect, nanoplates generated contrast 4 times brighter at the tumor site than the tissue before the injection (Fig. 14).

In 2012, Homan *et al.* first reported the application of silver nanoplates as a contrast agent for molecular PA imaging.[210] The authors prepared triangular Ag nanoplates by a seeded-growth method with tunable LSPR from the visible up to the NIR. To detect by PA imaging the active-targeted accumulation of nanoplates in tumors, an anti-epidermal growth factor receptor (a-EGFR) antibody was conjugated on PEGylated nanoprisms, successively injected into the tail vein of Nu/Nu transgenic mice with xenograft human pancreatic cancer grown orthotopically. At 4 h post injection, the maximum accumulation in the tumor was observed by monitoring PA signal over time. Overall, this study revealed the applicability of Ag nanoplates as a PA contrast agent and their potential use for bioimaging and sensing.

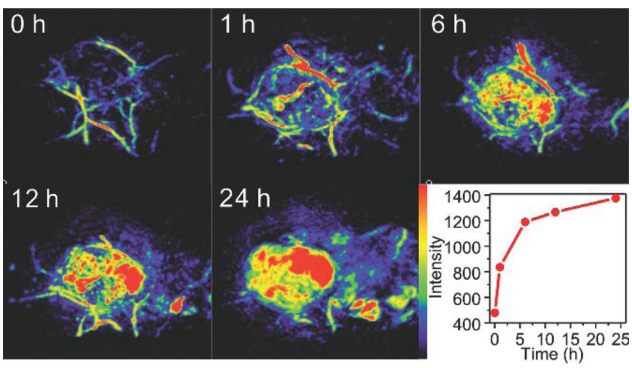

Fig. 14 PA imaging of tumors in mice before and 1, 6, 12 and 24 h after the intravenous injection of PEGylated Pd@Au nanoplates. Adapted from ref. 209.

Lately, Cha *et al.* have described the preparation of silica-coated silver bumpy nanoshells (AgNSs@SiO_2) for SERS and PA imaging of SLNs *in vivo*.[211] AgNSs have displayed strong scattering properties in the NIR with an absorption peak at 680 nm, and higher SERS enhancement compared to gold nanorods or nanospheres. For this reason, AgNSs have been first labeled with various Raman probes and then embedded in SiO_2 shells and surface-stabilized with bovine serum albumin (BSA) for PA imaging at 680 nm and SERS. PA has been performed on female rats, enabling contrast at the SLN 3.3 and 3.8 times more intense than the response of hemoglobin from the surrounding vessels at 40 and 160 min of the injection, respectively. SERS results confirmed strong accumulation on SLN *in vivo*. Nano-silver has been widely studied in the last few decades thanks to its well-known biocompatibility and antibacterial properties; herein, it has been demonstrated how, similarly to gold, its longitudinal LSPR can be finely tuned in the NIR for application in PA imaging and photothermal therapy. However, nanostructures of this metal require larger sizes and more complex shapes to achieve high absorption coefficients in the biological windows.

In 2017, He *et al.* documented the application of titanium nitride nanoparticles (TiN NPs) as a novel theranostic platform for PA imaging and PTT.[212] Compared to gold and silver, the LSPR of titanium is significantly red-shifted and strong absorptions in the NIR can be obtained without the need for complex architectures.[213] The authors obtained 20 nm particles with broad absorption in the NIR and poor cytotoxicity *in vitro* and suggested their application in PA imaging and PTT. For these reasons, tumor-bearing mice were injected with PEGylated TiN NPs in their jugular vein and PA imaging was performed at the tumor site. PA images showed 150% signal enhancement at the tumor site 24 h after the injection, suggesting effective tumor accumulation. PTT results confirmed the potential of Pt as a theranostic platform for PA imaging.

Carbon nanomaterials

Basic work on the application of single-walled carbon nanotubes (SWNTs) for PA imaging was performed by de la Zerda *et al.* between 2008 and 2012.[214–216] Firstly, it has been described how RGD-conjugated carbon nanotubes could serve as a contrast agent for PA imaging of tumors *in vivo*. They obtained SWNTs of 1–2 nm in diameter and 50–300 nm in length, which showed strong NIR absorption between 690 nm and 790 nm and linear correlation between concentration and PA signal intensity *in vitro*. Hence, to evaluate the effective PA contrast obtainable *in vivo*, 200 μL of 1.2 μM RGD-conjugated SWNTs have been injected into the tail vein of U87MG xenograft tumor-bearing mice. PA 3D images acquired before and 4 h after the injection showed an 8-fold increase in the PA

signal compared to the system pre-injection. Successively, in 2010, they reported an improvement of their contrast thanks to the conjugation of ICG to nanotubes. This has allowed a strong increase in the PA contrast *in vivo* (300×) compared to their previous work, but in this case the signal mainly originates from abundant ICG on the SWNT backbone. Finally, in 2012, the authors further extended their studies on the comparison between nanotubes conjugated to different NIR dyes for *in vivo* PA experiments, which revealed that stronger NIR absorber dyes allowed for brighter PA contrast.

Later, Chen *et al.* presented PEGylated single-walled carbon nanohorns (SWNHs) with improved stability and biocompatibility as a photothermal agent and for PA imaging both *in vitro* and *in vivo*.[217] Their SWNHs presented broad and intense absorption in the NIR, well-suited for PA imaging and PTT. After the assessment of their non-toxicity, the authors injected 200 μL of 2 mg mL^{-1} PEGylated carbon nanohorns in tumor-bearing mice and PA signal was monitored at the tumor site before and up to 48 h after the injection. The PA signal reached its maximum 24 h post-injection with a signal enhancement factor of around 6, suggesting the involvement of slow processes, such as EPR, in the accumulation of contrast in the tumor (Fig. 15). In addition, the proposed nanoconstructs showed remarkable results as PTT agents, thanks to their high light-to-heat conversion efficiency, also exploited in PA imaging.

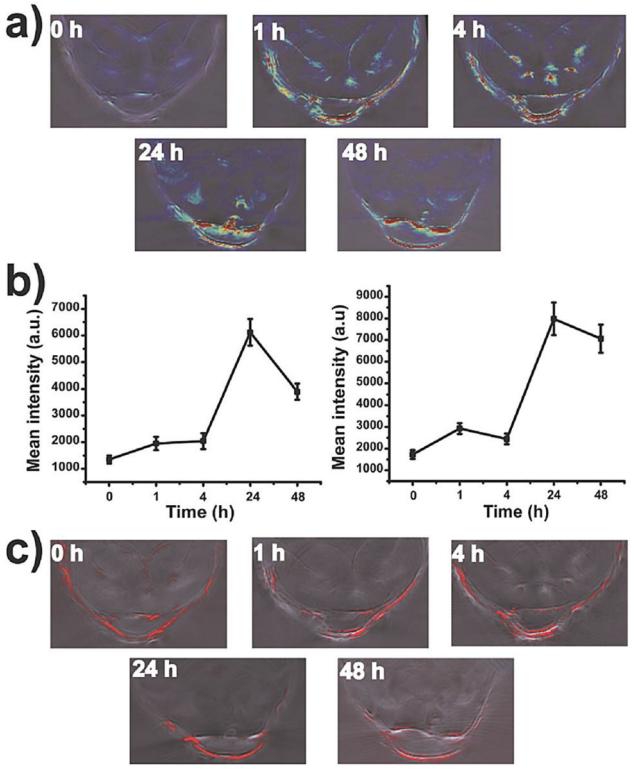

Fig. 15 *In vivo* PA images of tumor bearing mice intravenously injected with PEGylated SWNHs. (a) PA signal from nanohorns before and 1 h, 4 h, 24 h and 48 h after the injection, showing clear accumulation in the tumor. (b) The mean PA signal intensity at the tumor site over time. Maximum accumulation was observed 24 h after the injection. (c) PA images of hemoglobin (Hb) in the tumor at different time steps after the administration. Adapted from ref. 217.

Fullerenes appeared in the field of PA contrast agents when Krishna *et al.* proposed it in 2010 using polyhydroxyfullerenes (PHFs) for PA imaging of tumors.[218] Water-soluble PHF and chitosan-encapsulated PHF nanoparticles have shown good PA contrast *in vitro* and negligible cytotoxicity, suggesting their potential use in PTT and PA imaging *in vivo*. Hence, BT474 tumor cell-bearing mice have been intratumorally injected with 30 μL of PHF 10 mg mL^{-1} or 0.45 mg mL^{-1} of PHF-functionalized chitosan nanoparticles before undergoing PA imaging analysis in the tumor region. Both injections showed good contrast at the tumor site compared to control experiments, generating signals as high as 4–5 times the endogenous response.

Notwithstanding their promising contrast abilities, good absorption coefficients and low reported toxicity, both carbon nanotubes and PHFs display broad absorption throughout the visible and the NIR: this can hamper the employment of multispectral approaches for the discrimination of exogenous contrast from the endogenous one, generating wavelength-independent contrast.

Graphitic carbon nanoparticles from natural sources were prepared in 2013 by Wu *et al.* from honey in a domestic microwave.[219] The authors microwaved a dispersion of one macromolecular passivating agent (PEG or polysorbate) in honey under an Ar atmosphere for 10–30 min, obtaining 7 nm luminescent carbon nanoparticles or carbon dots (OCNs). The particles showed broad absorption throughout the NIR; thus their PA properties towards the identification of SLNs have been tested. After the assessment of the *in vitro* potential of carbon dots as PA contrast agents, 650 nm was chosen as the best excitation wavelength to maximize the signal-to-noise ratio. 1–2 min after the intravenous injection of 100 μL of 25%$_{vol}$ OCNs solution into living mice, PA images of the femoral vessels have been acquired *in vivo*, showing a 60-fold PA signal enhancement at the SLN right after the injection, which rapidly decreased due to poor nanoparticle retention at the lymph node.

Recently, Wu *et al.* deeply investigated PA contrast generated by porphyrin-containing carbon nanodots (C-Dots).[220] In particular, the authors conducted a partial hydrolysis of 5,10,15,20-tetrakis(4-aminophenyl)porphyrin (TAPP) and citric acid to afford carbon dots with strong UV-visible and NIR absorption. Reactive carboxylic moieties from citric acid were observed to be directed towards the surface of the particles, allowing for EDC-assisted amide coupling with α,ω-diamino PEG. Hence, the carboxylic terminus of the C225 antibody has been coupled to the C-Dots surface to exploit the high binding affinity of the antibody for the epidermal growth factor receptor (EGFR), allowing for active targeting. PA imaging analysis *in vitro* revealed that deprotonation of the porphyrin induced by alkaline pH completely inhibits the light absorption properties of the system, suggesting the possibility of obtaining PA contrast triggered by the intrinsic acidity of cancer cells.

As has been reviewed in detail, graphitic carbon nanostructures offer good PA contrast and improved biocompatibility, despite displaying visible rather than NIR absorption and very small size. Moreover, the molar absorption coefficient and photothermal conversion efficiency of carbon nanoparticles are rarely evaluated, making it hard to compare their performances with different nanostructures showing similar physical–chemical features.

Finally, nanodiamonds have been studied by Zhang *et al.* for their potential application as a PA contrast agent of tissues.[221] Nanodiamonds (NDs) have been prepared by ion irradiation of natural diamond powder at high dosage to create the vacancies required for electronic transition, and thus absorption, to occur. After *in vitro* and *ex vivo* PA imaging tests to assess the pure contrast from nanodiamonds, *in vivo* experiments were conducted. NDs have been subcutaneously injected into the lower back of a mouse, revealing 919% signal enhancement at the injection site and 567% contrast for a 3 mm deep injection. However, despite the promising results about nanodiamonds' cytotoxicity, the complexity of the synthesis procedure makes NDs hardly employable in the clinics on a large scale.

Polymeric nanostructures

In two consecutive studies from 2014 and 2015, Pu *et al.* amply described the performances of engineered semiconducting polymer nanoparticles (SPNs) for preclinical PA imaging.[222,223] In their first work, they reported a NIR-activatable PA probe for the detection of the progression of pathological processes. Poly(cyclopentadithiophene-*alt*-benzothiadiazole) had been chosen to build SPNs by surfactant-assisted nanoprecipitation because of its strong absorption in the NIR, suitable for PA and fluorescence imaging. The nanoparticles displayed an absorption peak at 660 nm, with a mass absorption coefficient of 93 mL mg^{-1} cm^{-1}. The PA performances of SPNs have been evaluated in comparison with GNRs and SWNTs, both *in vitro* and *in vivo*; 50 μg of nanoparticles were injected into mice for lymph node tracking by PA and fluorescence detection. The recorded amplitude of the PA signal increased by a factor of 10 after administration, allowing the clear visualization of several lymph nodes in the region of injection, confirmed by fluorescence imaging from the SPNs. The obtained PA amplitudes for SPNs have been found to be 4 times greater than the ones recorded for GNRs and SWNTs on a mass basis (Fig. 16).

Moreover, by nanoprecipitating a semiconducting polymer with IR775S, a NIR dye sensitive to reactive oxygen species (ROS), the authors built a smart PA nanoprobe whose PA spectrum was sensitive to endogenously generated ONOO- and OCl- *in vivo*. Later, the same authors reported a new series of diketopyrrolopyrrole-based SPNs for *in vivo* PA imaging of tumor, as a proof-of-concept. The SPNs with the best perform-

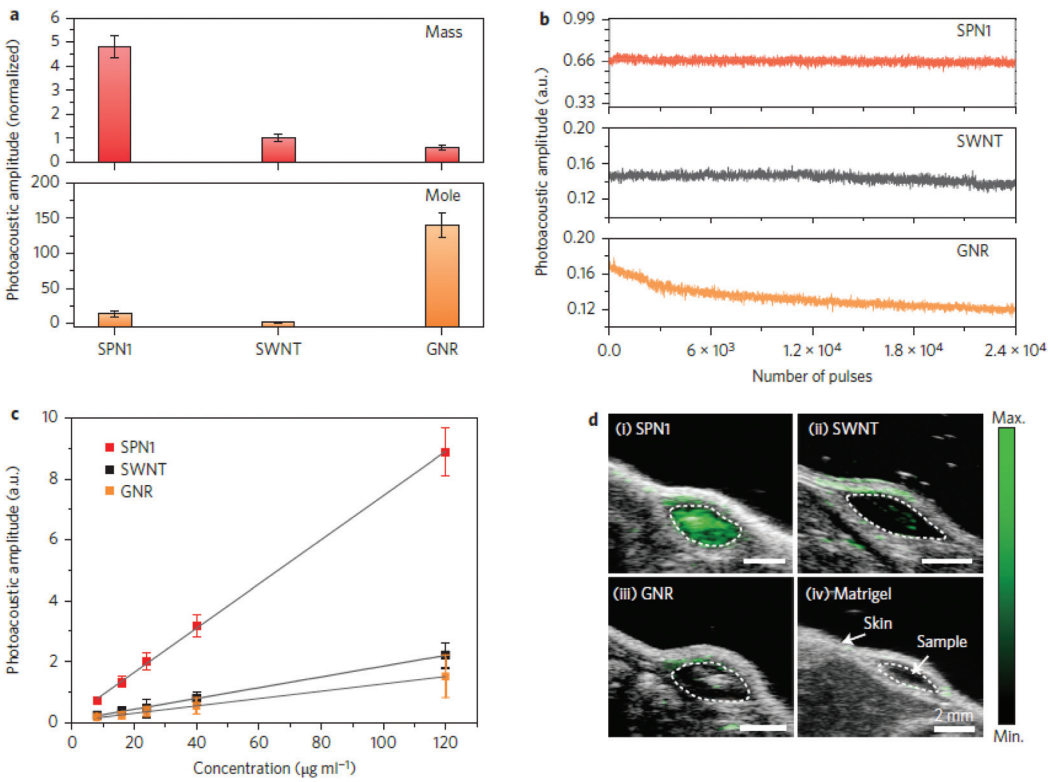

Fig. 16 Comparison between the PA performances of SPNs, gold nanorods (GNRs) and SWNTs. (a) Normalized PA amplitude by mass or by mole. (b) Nanoparticle signal stability with prolonged irradiation for the three systems. SPNs display constant PA emission, while GNRs are less stable due to reshaping phenomena. (c) Calibration curves for PA contrast *vs.* concentration *in vitro*. (d) Recorded PA images at the site of injection of Matrigel-included nanoparticles at 8 μg mL^{-1} concentration. Adapted from ref. 222.

ances have been chosen out of 3 different polymers for PA imaging *in vivo*, revealing strong contrast at the tumor site up to 24 h post-injection. Remarkable results were obtained by Huynh *et al.* in 2015 when they described the production of convertible porphyrin microbubbles (pMBs) for multimodal PA/US imaging.[224] They first built micellar microbubbles encapsulating perfluorocarbon gas using the porphyrin-containing bacteriochlorophyll–lipid (BChl-lipid), generating a microparticle displaying US contrast due to the high acoustic impedance of gasses and PA and fluorescence imaging due to absorption from porphyrin groups. Moreover, by exposure to low-frequency US waves, the microbubbles were transformed into smaller particles (5–500 nm) with the same optical properties as the former. After the stability of the PA contrast had been assessed *in vitro*, tumor-bearing mice were injected with 150 μL of 8.4×10^7 pMBs solution to study and verify PA contrast and the micro-to-nano transformation by PA imaging.

More recently, Lyu reported a new theranostic nanoplatform based on semiconducting polymers for PA imaging and PTT.[225] Molecularly-engineered poly[2,6-(4,4-bis(2-ethylhexyl)-4*H*-cyclopenta-[2,1-*b*;3,4-*b*′]dithiophene)-*alt*-4,7-(2,1,3-benzothiadiazole)] (PCPDTBT) and (6,6)-phenyl-C71-butyric acid methyl ester (PC70BM) nanoparticles have been prepared by nanoprecipitation. PCPDBTB is a semiconducting polymer with absorption in the NIR (840 nm), while PC70BM is a highly electrophilic and hydrophilic fullerene that enables intramolecular PET contrast. Thanks to HOMO–LUMO coupling between the polymer and the fullerene units, increasing amounts of fullerenes caused sensitive increment of PA signal in the NIR. Hence, 200 μL of 100 μg mL^{-1} nanoparticle solution have been systemically injected into 4T1 tumor-bearing mice, and PA images have been acquired 6 h post-injection. Images revealed 1.8× PA signal enhancement for SPNs compared to the injection of control nanoparticles. The nanoconstruct also allowed for fluorescence imaging and PTT showing promising results as a carbon-based biocompatible theranostic platform.

The same year, Jiang described semiconducting polymer nanoparticles with absorption in both the biological windows in the NIR.[226] SPNs were built by nanoprecipitation of a mixture of poly[diketopyrrolopyrrole-*alt*-thiophene] and poly(diketopyrrolopyrrole-*alt*-thiadiazoloquinoxaline) with PEG-*b*-PPG-*b*-PEG as a stabilizer. The obtained SPNs displayed broad NIR absorption at 744 nm and 1253 nm, allowing for NIR dual-wavelength PA imaging for more accurate localization in living tissues. As a proof-of-concept, *in vivo* PA imaging of the rat brain vasculature was performed on a homemade PA system equipped with two lasers, at 750 nm and 1064 nm. PA signal remarkably increased at 750 nm after the intravenous injection of 300 μL of 6 mg mL^{-1}, but contrast at 1064 nm was 1.5 times stronger. These results demonstrate that SPNs can serve as a PA contrast agent in the second biological window of the electromagnetic spectrum, where high penetration depth can be achieved.

To sum up, semiconducting conjugated polymers offer the possibility to employ full-organic self-assembling materials for generating efficient PA contrast *in vivo* in a wide spectral range. However, thanks to the rigid conjugated structure of the polymers, fluorescence phenomena widely occur upon NIR laser excitation. Therefore, detailed studies on the photothermal conversion efficiencies should be conducted on different SPNs to evaluate their effective PA contrast ability. Moreover, detailed studies on the possible metabolic pathways involving SPNs should be conducted to evaluate the possible toxicity of cleaved monomers circulating in the body.

As a first application of protein-based PA contrast, Li *et al.* developed a genetically encoded small NIR photochromic protein capable of a strong PA effect, and a novel approach for the application of PA imaging to the study of protein interactions *in vivo*.[227] In this work, the authors employed temporal unmixing to discriminate PA signals from cells distributed at different depths in biological systems. The different photophysical behavior of two different long-wavelength absorbing bacterial phytochromes, RpBphP1 from *Rhodopseudomonas palustris* and DrBphP-PCM from *Deinococcus radiodurans*, have been exploited to develop a reversibly switchable PA computed tomography system (RS-PACT) combined with single-impulse panoramic PA imaging (SIP-PACT) and real-time detection of genetically encoded NIR-absorbing protein probes. Briefly, U87 cells expressing the bacterial phytochrome DrBphP-PCM have been injected in the right lobe of a living mouse liver, followed by the injection of HEK-293 cells, engineered to express both the bacterial phytochromes in the left lobe of the organ. By exploiting the different decay profiles of the PA signal of the two proteins over time, signals coming from the different photoemitters have been efficiently separated. Furthermore, DrBphP-PCM has been split into two of its main components, named DrPAS and DrGAF-PHY, to achieve PA contrast only when the two domains reconnected to form the photoresponsive core. By connecting the two distinct domains to different interacting proteins and exploiting the photoswitching properties of the engineered system, the split phytochrome DrSplit has been employed to efficiently study protein–protein interactions (PPI) *in vivo*.

Hybrid nanocomposites

In this last section, we review complex hybrid nanosystems composed of two or more different nanostructured sub-units, capable of efficient PA contrast. These represent the most advanced developments in the field, allowing for extremely tunable responses and enhanced contrast due to the combination of the thermal expansions of the single components.

In 2009, Kim *et al.* reported the preparation of golden carbon nanotubes (GNTs) as a biocompatible theranostic platform for simultaneous PA-PT microscopy to overcome the limitations in toxicity and absorption for carbon nanomaterials by taking advantage of the strong optical absorption and consolidated biocompatibility of gold.[228] The authors prepared GNTs by depositing a 4–8 nm thick gold layer onto SWNTS by slow reduction of $HAuCl_4$ with no need for external reductants. Similar to GNRs, GNTs showed longitudinal and transverse LSPR absorption, at 520–530 nm and 850 nm,

respectively, comparable with gold nanorods with an aspect ratio of around 4–5. GNTs have been further conjugated with an anti-LYVE-1 antibody for the evaluation of actively targeted accumulation of contrast *in vivo*. Anti-LYVE-1 had been previously reported to specifically bind lymphatic endothelial cells (LECs) lying on the internal surface of lymphatic vessels; thus conjugation should have ensured contrast from lymphatic vessels. After the introduction of the GNTs into the lymphatic system of living mice, simultaneously acquired PA/PT microscopic images revealed a 70-fold enhancement in the PA signal at its maximum (1 h post-injection), allowing for noiseless visualization of lymphatics in the mesentery.

In addition, Liu *et al.* have in 2013 described the implementation of Au–$Cu_{2-x}Se$ heterodimer nanoparticles as a plasmonic–semiconducting hybrid contrast agent for *in vivo* PA imaging.[229] Nanoparticles have been obtained using gold nanoparticles as seeds for the seeded growth of $Cu_{2-x}Se$ nanocrystals. The interaction between plasmonic and semiconducting domains generates broad absorption across both the visible and the NIR, up to 1750 nm. The change in PA signal was monitored in the axillary vasculature rats (at 1064 nm) after successive intravenous injection of 200 μL of 4 mg mL^{-1} Au–$Cu_{2-x}Se$ nanocrystals, showing 200% contrast enhancement 1 h after the first injection and 290% 1 h after the second injection.

Later, Wang *et al.* employed PA imaging for the detection of gastric cancer using RGD-conjugated SiO_2-coated gold nanorods (sGNRs) on the surface of multiwalled carbon nanotubes (MWNTs).[230] The two nanostructures have been coupled *via* amide bond formation between amino groups on sGNRs and the carboxylic residues on MWNTs. The absorption spectrum of MWNTs/sGNRs displayed broad absorption in the NIR, with the LSPR peak from GNRs still present at 680 nm. Contrast efficiency was tested *in vivo* by PA imaging of a subcutaneous gastric cancer xenograft model in mice, showing contrast enhancement and accumulation at the tumor site up to 12 h post-injection. Moreover, 20% PA signal enhancement has been confirmed to be a consequence of sGNR interaction with MWNTs at the quantum level in the hybrid nanostructure.

The same type of interaction at the nanoscale was also explored later on when Moon *et al.* described their experiments with reduced graphene oxide coated gold nanorods (r-GO-GNRs) for PA imaging.[231] In their work, the authors studied the enhanced NIR absorption properties ($\lambda_{max} \approx$ 750 nm) of r-GO-GNRs and confirmed their excellent photothermal stability and photoacoustic efficiency. Furthermore, to prove the promising PA contrast *in vivo*, 50 μL of 1.25 nM r-GO-GNRs have been dispersed in Matrigel and injected into the back of mice. PA imaging at the injection site (at 750 nm) revealed a 40-fold signal enhancement from the composite nanostructure (Fig. 17).

Then, Gao in 2016 reported the PA performances of a different Au-graphene hybrid as an activatable theranostic agent.[232] Their nanoconstruct was based on the GO-Au nanoparticle nanocomposite that was covalently connected to the matrix metalloprotease-14 (MMP-14) labeled with a NIR dye. PA imaging revealed a significant contrast *in vivo* compared to AuNPs and GO alone, as reported previously. The PA enhancement due to the coupling between gold and carbon is believed to be due to fluorescence quenching from gold towards GO, which causes an increase in the photoacoustic efficiency of the graphene sheets. More recently, Chen *et al.* described the

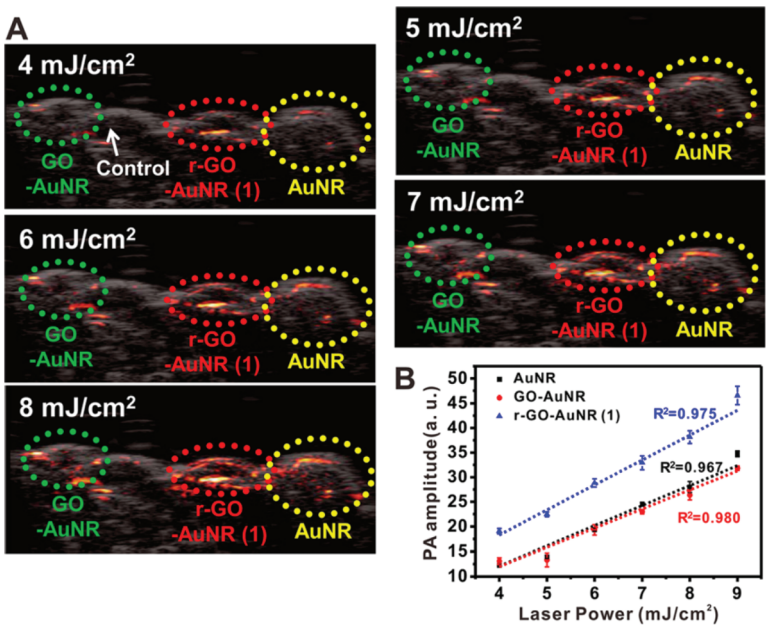

Fig. 17 *In vivo* PA imaging experiments on GNRs, GO-GNRs and r-GO-GNRs. (A) PA images of the injection sites obtained by changing the laser power from 4 to 9 mJ cm^{-2}. (B) Linear relationship between PA amplitude and laser power; r-GO-GNRs display stronger PA amplitude and higher sensitivity towards variations in laser power. Adapted from ref. 231.

preparation of composite nanomodulators for dynamic contrast-enhanced PA imaging.[233] The authors prepared poly(*n*-isopropylacrylamide) (PNIPAM) nanogels loaded with GNRs and CuS QDs. The two nanosystems have been compared on several aspects, such as optical cross-section, absorption tunability, size and photostability. Dynamic contrast-enhanced imaging allows separating static background signals from dynamic signals from the contrast, hence increasing the signal-to-noise ratio and allowing for unambiguous identification of the contrast.

In 2018, we reported the production of a triple-modality imaging probe based on $MnFe_2O_4$ nanoparticles, GNRs and fluorescein, allowing for unambiguous contrast detection *in vivo*.[234] Silica-coated magnetic nanoparticles have been functionalized with amino- and azido-modified silanes, further coupled *via* click chemistry to alkyne-functionalized GNRs, to achieve a smart assembly capable of triple fluorescence, MRI and PA imaging contrast *in vivo*. We evaluated PA signals by injection of a few microliters of a nanoprobe solution in chicken breast tissue, revealing good contrast and high signal-to-noise ratio even at concentrations as low as 34 μM, which corresponded to a 50-fold PA signal enhancement compared to the background. Moreover, the PA signal coming from the thermoelastic expansion of GNRs was observed to be constant with time, revealing no reshaping involving the gold nanostructure.

The outstanding properties of these latest examples demonstrate the possibility to covalently combine the PA features of different nanostructures to nanomaterials that display very different properties, allowing for the fabrication of advanced nanocomposites with unique diagnostic efficacies. However, the interactions of the combined nanosystems in a biological environment should be evaluated in each case, and the stability of the connections between independent blocks must be ensured to avoid leakage of some of the components of the hybrid nanocomposites.

Conclusions

In conclusion, nanostructured contrast agents have been reported to be capable of making PA imaging an efficient tool for the noninvasive visualization of superficial and deep tissues. The appropriate contrast agent should be chosen for each application according to its optical properties, biocompatibility and photostability, and it can be engineered in a large variety of ways to couple PA imaging to other imaging modalities. Contrast agents for PA imaging can often serve as PTT agents, thus representing good candidates as theranostic platforms against cancer. However, more concern should be directed towards detailed and representative biocompatibility studies not only for each class of contrast agents, but for each single nanosystem. Parameters such as particle size, shape, surface charge, coating and roughness are key parameters for determining the toxicity mechanism of nanomaterials and their path in complex biosystems. For example, preliminary pharmacokinetics studies reveal that spherical gold nanoparticles can cause cell division dysfunctions while cylindrical gold nanorods are related to chronic inflammation.[235] Nowadays, the main limitations concerning contrast media for PA imaging are related to the long-term toxicity and biodistribution of the nanostructures after administration and their stability upon prolonged irradiation.

Thus, detailed studies are yet to be conducted, but preliminary studies confirm the promising features of several nanostructures for *in vivo* applications. Moreover, contrast-based PA imaging could be employed in the near future for clinical trials on humans, highlighting the need for contrast agents to achieve deeper tissue penetration and higher photostability.

In perspective, by analysing the market trend in developing novel contrast agents, which is continuously growing, and in consideration of the fact that PA is an easy, portable, low cost imaging technique that can be coupled with commonly and largely distributed echographic instrumentation, a future increase of PA applications can be expected together with an improvement in contrast agent development, specificity and applicability.

Conflicts of interest

There are no conflicts to declare.

Acknowledgements

This work has received funding from H2020 FETOPEN-2016-2017 (no. 801126, EDIT project 236–238).

Notes and references

1 T. N. Erpelding, A. Garcia-Uribe, A. Krumholz, H. Ke, K. Maslov, C. Appleton, J. Margenthaler and L. V. Wang, *Photons Plus Ultrasound: Imaging and Sensing*, 2014, **8943**, 894359.
2 M. Xu and L. V. Wang, *Rev. Sci. Instrum.*, 2006, **77**, 041101.
3 J. Weber, P. C. Beard and S. E. Bohndiek, *Nat. Methods*, 2016, **13**, 639–650.
4 A. M. Smith, M. C. Mancini and S. Nie, *Nat. Nanotechnol.*, 2009, **4**, 710–711.
5 Y. Lao, D. Xing, S. Yang and L. Xiang, *Phys. Med. Biol.*, 2008, **53**, 4203–4212.
6 L. J. Rich and M. Seshadri, *Radiology*, 2015, **275**, 110–118.
7 Q. Shao, E. Morgounova, C. Jiang, J. Choi, J. Bischof and S. Ashkenazi, *J. Biomed. Opt.*, 2013, **18**, 076019.
8 M. Gerling, Y. Zhao, S. Nania, K. J. Norberg, C. S. Verbeke, B. Englert, R. V. Kuiper, Å. Bergström, M. Hassan, A. Neesse, J. M. Löhr and R. L. Heuchel, *Theranostics*, 2014, **4**, 604–613.
9 S. Mallidi, K. Watanabe, D. Timerman, D. Schoenfeld and T. Hasan, *Theranostics*, 2015, **5**, 289–301.
10 T. J. Allen, A. Hall, A. P. Dhillon, J. S. Owen and P. C. Beard, *J. Biomed. Opt.*, 2012, **17**, 061209.

11 J. A. Guggenheim, T. J. Allen, A. Plumb, E. Z. Zhang, M. Rodriguez-Justo, S. Punwani and P. C. Beard, *J. Biomed. Opt.*, 2015, **20**, 050504.
12 I. Stoffels, S. Morscher, I. Helfrich, U. Hillen, J. Leyh, N. C. Burton, T. C. P. Sardella, J. Claussen, T. D. Poeppel, H. S. Bachmann, A. Roesch, K. Griewank, D. Schadendorf, M. Gunzer and J. Klode, *Sci. Transl. Med.*, 2015, **7**, 317ra199.
13 Q. Fan, K. Cheng, X. Hu, X. Ma, R. Zhang, M. Yang, X. Lu, L. Xing, W. Huang, S. S. Gambhir and Z. Cheng, *J. Am. Chem. Soc.*, 2014, **136**, 15185–15194.
14 P. Wang, P. Wang, H.-W. Wang and J.-X. Cheng, *J. Biomed. Opt.*, 2012, **17**, 0960101.
15 P. Wang, J. R. Rajian and J. X. Cheng, *J. Phys. Chem. Lett.*, 2013, **4**, 2177–2185.
16 Gd. View Res., 2018, 1–8.
17 R. E. Borg and J. Rochford, *Photochem. Photobiol.*, 2018, **94**, 1175–1209.
18 C. Brückner, *Photochem. Photobiol.*, 2018, 1–3.
19 R. C. Benson and H. A. Kues, *Phys. Med. Biol.*, 1978, **23**, 017.
20 W. M. Kuebler, *J. Appl. Physiol.*, 2008, **104**, 905–906.
21 Z. Sheng, D. Hu, M. Xue, M. He, P. Gong and L. Cai, *Nano-Micro Lett.*, 2013, **5**, 145–150.
22 X. Wang, G. Ku, M. A. Wegiel, D. J. Bornhop, G. Stoica and L. V. Wang, *Opt. Lett.*, 2004, **29**, 730–732.
23 A. Miyata, T. Ishizawa, M. Kamiya, A. Shimizu, J. Kaneko, H. Ijichi, J. Shibahara, M. Fukayama, Y. Midorikawa, Y. Urano and N. Kokudo, *PLoS One*, 2014, **9**, e112667.
24 K. Kanazaki, K. Sano, A. Makino, T. Homma, M. Ono and H. Saji, *Sci. Rep.*, 2016, **6**, 33798.
25 C. Lutzweiler, R. Meier, E. Rummeny, V. Ntziachristos and D. Razansky, *Opt. Lett.*, 2014, **39**, 4061–4064.
26 K. Sano, M. Ohashi, K. Kanazaki, N. Ding, J. Deguchi, Y. Kanada, M. Ono and H. Saji, *Biochem. Biophys. Res. Commun.*, 2015, **464**, 820–825.
27 J. P. Tardivo, A. Del Giglio, C. S. De Oliveira, D. S. Gabrielli, H. C. Junqueira, D. B. Tada, D. Severino, R. De Fatima Turchiello and M. S. Baptista, *Photodiagn. Photodyn. Ther.*, 2005, **2**, 175–191.
28 K. H. Song, E. W. Stein, J. A. Margenthaler and L. V. Wang, *J. Biomed. Opt.*, 2008, **13**, 054033.
29 C. Kim, M. Jeon and L. V. Wang, *Opt. Lett.*, 2011, **36**, 3599.
30 W. J. Akers, W. B. Edwards, C. Kim, B. Xu, T. N. Erpelding, L. V. Wang and S. Achilefu, *Transl. Res.*, 2012, **159**, 175–181.
31 U. Mayerhöffer, B. Fimmel and F. Würthner, *Angew. Chem., Int. Ed.*, 2012, **51**, 164–167.
32 Y. Y. Zhang, M. Jeon, L. J. Rich, H. Hong, J. Geng, Y. Y. Zhang, S. Shi, T. E. Barnhart, P. Alexandridis, J. D. Huizinga, M. Seshadri, W. Cai, C. Kim and J. F. Lovell, *Nat. Nanotechnol.*, 2014, **9**, 631–638.
33 C. Lee, J. Kim, Y. Zhang, M. Jeon, C. Liu, L. Song, J. F. Lovell and C. Kim, *Biomaterials*, 2015, **73**, 142–148.
34 C. J. H. Ho, G. Balasundaram, W. Driessen, R. McLaren, C. L. Wong, U. S. Dinish, A. B. E. Attia, V. Ntziachristos and M. Olivo, *Sci. Rep.*, 2015, **4**, 5342.
35 A. Ray, X. Wang, Y. E. K. Lee, H. J. Hah, G. Kim, T. Chen, D. A. Orringer, O. Sagher, X. Liu and R. Kopelman, *Nano Res.*, 2011, **4**, 1163–1173.
36 C. Yin, Y. Tang, X. Li, Z. Yang, J. Li, X. Li, W. Huang and Q. Fan, *Small*, 2018, **14**, 1703400.
37 W. J. Akers, C. Kim, M. Berezin, K. Guo, R. Fuhrhop, G. M. Lanza, G. M. Fischer, E. Daltrozzo, A. Zumbusch, X. Cai, L. V. Wang and S. Achilefu, *ACS Nano*, 2011, **5**, 173–182.
38 Y. Ni, R. K. Kannadorai, J. Peng, S. W.-K. Yu, Y.-T. Chang and J. Wu, *Chem. Commun.*, 2016, **52**, 11504–11507.
39 E. Huynh, J. F. Lovell, B. L. Helfield, M. Jeon, C. Kim, D. E. Goertz, B. C. Wilson and G. Zheng, *J. Am. Chem. Soc.*, 2012, **134**, 16464–16467.
40 X. Liang, Z. Deng, L. Jing, X. Li, Z. Dai, C. Li and M. Huang, *Chem. Commun.*, 2013, **49**, 11029.
41 S. Shi, Y. Liu, Y. Chen, Z. Zhang, Y. Ding, Z. Wu and J. Yin, *Theranostics*, 2016, **6**(12), 2170–2182.
42 D. Zhang, Y.-X. Zhao, Z.-Y. Qiao, U. Mayerhöffer, P. Spenst, X.-J. Li, F. Würthner and H. Wang, *Bioconjugate Chem.*, 2014, **25**, 2021–2029.
43 S. Bellinger, M. Hatamimoslehabadi, R. E. Borg, J. La, P. Catsoulis, F. Mithila, C. Yelleswarapu and J. Rochford, *Chem. Commun.*, 2018, **54**, 6352–6355.
44 Y. Jiang and K. Pu, *Adv. Biosyst.*, 2018, **2**, 1700262.
45 A. L. Doiron, K. A. Homan, S. Emelianov and L. Brannon-Peppas, *Pharm. Res.*, 2009, **26**, 674–682.
46 Y. Kohl, C. Kaiser, W. Bost, F. Stracke, M. Fournelle, C. Wischke, H. Thielecke, A. Lendlein, K. Kratz and R. Lemor, *Nanomedicine*, 2011, **7**, 228–237.
47 J. P. Thawani, A. Amirshaghaghi, L. Yan, J. M. Stein, J. Liu and A. Tsourkas, *Small*, 2017, **13**, 1–9.
48 N. Beziere, N. Lozano, A. Nunes, J. Salichs, D. Queiros, K. Kostarelos and V. Ntziachristos, *Biomaterials*, 2015, **37**, 415–424.
49 A. Hannah, G. Luke, K. Wilson, K. Homan and S. Emelianov, *ACS Nano*, 2014, **8**, 250–259.
50 H. Wang, C. Liu, X. Gong, D. Hu, R. Lin, Z. Sheng, C. Zheng, M. Yan, J. Chen, L. Cai and L. Song, *Nanoscale*, 2014, **6**, 14270–14279.
51 G. Kim, S.-W. Huang, K. C. Day, M. O'Donnell, R. R. Agayan, M. A. Day, R. Kopelman and S. Ashkenazi, *J. Biomed. Opt.*, 2007, **12**, 044020.
52 H.-W. An, S.-L. Qiao, C.-Y. Hou, Y.-X. Lin, L.-L. Li, H.-Y. Xie, Y. Wang, L. Wang and H. Wang, *Chem. Commun.*, 2015, **51**, 13488–13491.
53 H. D. Lu, B. K. Wilson, A. Heinmiller, B. Faenza, S. Hejazi and R. K. Prud'homme, *Appl. Mater. Interfaces*, 2016, **8**, 14379–14388.
54 Q. Chen, X. Liu, J. Chen, J. Zeng, Z. Cheng and Z. Liu, *Adv. Mater.*, 2015, **27**, 6820–6827.
55 L. Zhang, S. Gao, F. Zhang, K. Yang, Q. Ma and L. Zhu, *ACS Nano*, 2014, **8**, 12250–12258.

56 L. Xi, S. R. Grobmyer, G. Zhou, W. Qian, L. Yang and H. Jiang, *J. Biophotonics*, 2014, **7**, 401–409.
57 L. Jing, X. Liang, Z. Deng, S. Feng, X. Li, M. Huang, C. Li and Z. Dai, *Biomaterials*, 2014, **35**, 5814–5821.
58 Q. Mu, G. Su, L. Li, B. O. Gilbertson, L. H. Yu, Q. Zhang, Y. P. Sun and B. Yan, *ACS Appl. Mater. Interfaces*, 2012, **4**, 2259–2266.
59 A. R. Gliga, S. Skoglund, I. Odnevall Wallinder, B. Fadeel and H. L. Karlsson, *Part. Fibre Toxicol.*, 2014, **11**, 1–17.
60 F. G. Shellock and E. Kanal, *J. Magn. Reson. Imaging*, 1999, **10**, 477–484.
61 D. Wu, L. Huang, M. S. Jiang and H. Jiang, *Int. J. Mol. Sci.*, 2014, **15**, 23616–23639.
62 A. A. Oraevsky, *Photoacoustics*, 2015, **3**, 1–2.
63 P. Padmanabhan, A. Kumar, S. Kumar, R. K. Chaudhary and B. Gulyás, *Acta Biomater.*, 2016, **41**, 1–16.
64 M. Rai, A. P. Ingle, S. Birla, A. Yadav and C. A. Dos Santos, *Crit. Rev. Microbiol.*, 2015, 1–24.
65 E. C. Dreaden, A. M. Alkilany, X. Huang, C. J. Murphy and M. A. El-Sayed, *Chem. Soc. Rev.*, 2012, **41**, 2740–2779.
66 C. L. Nehl and J. H. Hafner, *J. Mater. Chem.*, 2008, **18**, 2415.
67 W. Li and X. Chen, *Nanomedicine*, 2015, **10**, 299–320.
68 D. L. Kokkin, R. Zhang, T. C. Steimle, I. A. Wyse, B. W. Pearlman and T. D. Varberg, *J. Phys. Chem. A*, 2015, **119**, 11659–11667.
69 C. Vericat, M. E. Vela, G. Benitez, P. Carro and R. C. Salvarezza, *Chem. Soc. Rev.*, 2010, **39**, 1805.
70 N. R. Panyala, E. M. Peña-Méndez and J. Havel, *J. Appl. Biomed.*, 2009, **7**, 75–91.
71 A. U. Borwankar, B. W. Willsey, A. Twu, J. J. Hung, R. J. Stover, T. W. Wang, M. D. Feldman, T. E. Milner, T. M. Truskett and K. P. Johnston, *RSC Adv.*, 2015, **5**, 104674–104687.
72 H. Deng, Y. Zhong, M. Du, Q. Liu, Z. Fan, F. Dai and X. Zhang, *Theranostics*, 2014, **4**, 904–918.
73 B. S. Gutrath, M. F. Beckmann, A. Buchkremer, T. Eckert, J. Timper, A. Leifert, W. Richtering, G. Schmitz and U. Simon, *Nanotechnology*, 2012, **23**, 225707.
74 R. Cheheltani, R. M. Ezzibdeh, P. Chhour, K. Pulaparthi, J. Kim, M. Jurcova, J. C. Hsu, C. Blundell, H. I. Litt, V. A. Ferrari, H. R. Allcock, C. M. Sehgal and D. P. Cormode, *Biomaterials*, 2016, **102**, 87–97.
75 P. Huang, J. Lin, W. Li, P. Rong, Z. Wang, S. Wang, X. Wang, X. Sun, M. Aronova, G. Niu, R. D. Leapman, Z. Nie and X. Chen, *Angew. Chem., Int. Ed.*, 2013, **52**, 13958–13964.
76 J. Song, J. Kim, S. Hwang, M. Jeon, S. Jeong, C. Kim and S. Kim, *Chem. Commun.*, 2016, **52**, 8287–8290.
77 T. Repenko, A. Rix, A. Nedilko, J. Rose, A. Hermann, R. Vinokur, S. Moli, R. Cao-Milàn, M. Mayer, G. von Plessen, A. Fery, L. De Laporte, W. Lederle, D. N. Chigrin and A. J. C. Kuehne, *Adv. Funct. Mater.*, 2018, **28**, 1–8.
78 Yu. S.-S. Chang, C.-L. Lee and C. R. C. Wang, *J. Phys. Chem. B*, 1997, **101**, 6661–6664.
79 X. Huang, I. H. El-Sayed, W. Qian and M. A. El-Sayed, *J. Am. Chem. Soc.*, 2006, **128**, 2115–2120.
80 X. Huang, S. Neretina and M. A. El-Sayed, *Adv. Mater.*, 2009, **21**, 4880–4910.
81 H. Chen, L. Shao, Q. Li and J. Wang, *Chem. Soc. Rev.*, 2013, **42**, 2679–2724.
82 S. Link and M. A. El-Sayed, *J. Phys. Chem. B*, 2005, **109**, 10531–10532.
83 S. Manohar, C. Ungureanu and T. G. Van Leeuwen, *Contrast Media Mol. Imaging*, 2011, **6**, 389–400.
84 H. Qin, T. Zhou, S. Yang, Q. Chen and D. Xing, *Nanomedicine*, 2013, **8**, 1611–1624.
85 H. W. Yang, H. L. Liu, M. L. Li, I. W. Hsi, C. T. Fan, C. Y. Huang, Y. J. Lu, M. Y. Hua, H. Y. Chou, J. W. Liaw, C. C. M. Ma and K. C. Wei, *Biomaterials*, 2013, **34**, 5651–5660.
86 F. Gao, L. Bai, S. Liu, R. Zhang, J. Zhang, X. Feng, Y. Zheng, Y. Zhao, Y. Zhao, Y. Ma, L. Cai, Z. Cheng, H. Dai, B. T. Khuri-Yakub and S. S. Gambhir, *Nanoscale*, 2017, **9**, 79–86.
87 J. Song, X. Yang, O. Jacobson, P. Huang, X. Sun, L. Lin, X. Yan, G. Niu, Q. Ma and X. Chen, *Adv. Mater.*, 2015, **27**, 4910–4917.
88 X. Tong, Z. Wang, X. Sun, J. Song, O. Jacobson, G. Niu, D. O. Kiesewetter and X. Chen, *Theranostics*, 2016, **6**, 2039–2051.
89 A. Agarwal, S. W. Huang, M. O'Donnell, K. C. Day, M. Day, N. Kotov and S. Ashkenazi, *J. Appl. Phys.*, 2007, **102**, 064701.
90 K. Kim, S.-W. Huang, S. Ashkenazi, M. O'Donnell, A. Agarwal, N. A. Kotov, M. F. Denny and M. J. Kaplan, *Appl. Phys. Lett.*, 2007, **90**, 223901.
91 M. Eghtedari, A. Oraevsky, J. A. Copland, N. A. Kotov, A. Conjusteau and M. Motamedi, *Nano Lett.*, 2007, **7**, 1914–1918.
92 J. W. M. Chon, C. Bullen, P. Zijlstra and M. Gu, *Adv. Funct. Mater.*, 2007, **17**, 875–880.
93 J. Comenge, O. Fragueiro, J. Sharkey, A. Taylor, M. Held, N. C. Burton, B. K. Park, B. Wilm, P. Murray, M. Brust and R. Lévy, *ACS Nano*, 2016, **10**, 7106–7116.
94 Y. S. Chen, W. Frey, S. Kim, P. Kruizinga, K. Homan and S. Emelianov, *Nano Lett.*, 2011, **11**, 348–354.
95 Z. Zhang, L. Wang, J. Wang, X. Jiang, X. Li, Z. Hu, Y. Ji, X. Wu and C. Chen, *Adv. Mater.*, 2012, **24**, 1418–1423.
96 S. J. Oldenburg, J. B. Jackson, S. L. Westcott and N. J. Halas, *Appl. Phys. Lett.*, 1999, **75**, 2897–2899.
97 T. C. Preston and R. Signorell, *ACS Nano*, 2009, **3**, 3696–3706.
98 L. Rouleau, R. Berti, V. W. K. Ng, C. Matteau-Pelletier, T. Lam, P. Saboural, A. K. Kakkar, F. Lesage, E. Rhéaume and J. C. Tardif, *Contrast Media Mol. Imaging*, 2013, **8**, 27–39.
99 E. FarrokhTakin, G. Ciofani, G. L. Puleo, G. de Vito, C. Filippeschi, B. Mazzolai, V. Piazza and V. Mattoli, *Int. J. Nanomed.*, 2013, **8**, 2319–2331.

100 J. Kim, S. Park, J. E. Lee, S. M. Jin, J. H. Lee, I. S. Lee, I. Yang, J.-S. Kim, S. K. Kim, M.-H. Cho and T. Hyeon, *Angew. Chem.*, 2006, **118**, 7918–7922.
101 J. E. Millstone, S. Park, K. L. Shuford, L. Qin, G. C. Schatz and C. A. Mirkin, *J. Am. Chem. Soc.*, 2005, **127**, 5312–5313.
102 J. E. Millstone, G. S. Métraux and C. A. Mirkin, *Adv. Funct. Mater.*, 2006, **16**, 1209–1214.
103 C. Bao, N. Beziere, P. Del Pino, B. Pelaz, G. Estrada, F. Tian, V. Ntziachristos, J. M. De La Fuente and D. Cui, *Small*, 2013, **9**, 68–74.
104 G. P. Luke, A. Bashyam, K. a. Homan, S. Makhija, Y.-S. Chen and S. Y. Emelianov, *Nanotechnology*, 2013, **24**, 455101.
105 J. Zhang, F. Xia, Y. Yang, C. Yue, C. Zhang, Y. Yang, L. Ma, G. Alfranca, Y. Liu, Y. Hou, W. Jin, J. Ni, J. M. de la Fuente and D. Cui, *Nano Biomed. Eng.*, 2016, **8**, 285.
106 X. Yang, S. E. Skrabalak, Z. Li, Y. Xia and L. V. Wang, *Nano Lett.*, 2007, **7**, 3798–3802.
107 G. D. Moon, S.-W. Choi, X. Cai, W. Li, E. C. Cho, U. Jeong, L. V. Wang and Y. Xia, *J. Am. Chem. Soc.*, 2011, **133**, 4762–4765.
108 W. Li, P. K. Brown, L. V. Wang and Y. Xia, *Contrast Media Mol. Imaging*, 2011, **6**, 370–377.
109 J. Chen, M. Yang, Q. Zhang, E. C. Cho, C. M. Cobley, C. Kim, C. Glaus, L. V. Wang, M. J. Welch and Y. Xia, *Adv. Funct. Mater.*, 2010, **20**, 3684–3694.
110 E. C. Cho, C. Kim, F. Zhou, C. M. Cobley, K. H. Song, J. Chen, Z. Y. Li, L. V. Wang and Y. Xia, *J. Phys. Chem. C*, 2009, **113**, 9023–9028.
111 K. H. Song, C. Kim, C. M. Cobley, Y. Xia and L. V. Wang, *Nano Lett.*, 2009, **9**, 183–188.
112 C. L. Nehl, H. Liao and J. H. Hafner, *Nano Lett.*, 2006, **6**, 683–688.
113 P. Pallavicini, A. Donà, A. Casu, G. Chirico, M. Collini, G. Dacarro, A. Falqui, C. Milanese, L. Sironi and A. Taglietti, *Chem. Commun.*, 2013, **49**, 6265.
114 A. A. Umar and M. Oyama, *Cryst. Growth Des.*, 2009, **9**, 1146–1152.
115 B. Lim and Y. Xia, *Angew. Chem.*, 2011, **50**, 76–85.
116 M. Hajfathalian, A. Amirshaghaghi, P. C. Naha, P. Chhour, J. C. Hsu, K. Douglas, Y. Dong, C. M. Sehgal, A. Tsourkas, S. Neretina and D. P. Cormode, *Nanoscale*, 2018, **10**, 18749–18757.
117 C. Pohling, J. L. Campbell, T. A. Larson, D. Van de Sompel, J. Levi, M. H. Bachmann, S. E. Bohndiek, J. V. Jokerst and S. S. Gambhir, *Small*, 2018, **14**, 1–10.
118 X. Michalet, F. F. Pinaud, L. A. Bentolila, J. M. Tsay, S. Doose, J. J. Li, G. Sundaresan, A. M. Wu, S. S. Gambhir and S. Weiss, *Science*, 2005, **307**, 538–544.
119 X. Gao, Y. Cui, R. M. Levenson, L. W. K. Chung and S. Nie, *Nat. Biotechnol.*, 2004, **22**, 969–976.
120 W. R. Algar, K. Susumu, J. B. Delehanty and I. L. Medintz, *Anal. Chem.*, 2011, **83**, 8826–8837.
121 B. Dubertret, P. Skourides, D. J. Norris, V. Noireaux, A. H. Brivanlou and A. Libchaber, *Science*, 2002, **298**, 1759–1762.
122 J. Mou, P. Li, C. Liu, H. Xu, L. Song, J. Wang, K. Zhang, Y. Chen, J. Shi and H. Chen, *Small*, 2015, **11**, 2275–2283.
123 K. Yang, L. Zhu, L. Nie, X. Sun, L. Cheng, C. Wu, G. Niu, X. Chen and Z. Liu, *Theranostics*, 2014, **4**, 134–141.
124 E. V. Shashkov, M. Everts, E. I. Galanzha and V. P. Zharov, *Nano Lett.*, 2008, **8**, 3953–3958.
125 X. Liu, W. C. Law, M. Jeon, X. Wang, M. Liu, C. Kim, P. N. Prasad and M. T. Swihart, *Adv. Healthcare Mater.*, 2013, **2**, 952–957.
126 W. Li, P. Rong, K. Yang, P. Huang, K. Sun and X. Chen, *Biomaterials*, 2015, **45**, 18–26.
127 L. Bouchard, M. S. Anwar, G. L. Liu, B. Hann, Z. H. Xie, J. W. Gray, X. Wang, A. Pines and F. F. Chen, *Proc. Natl. Acad. Sci. U. S. A.*, 2009, **106**, 4085–4089.
128 G. Ku, M. Zhou, S. Song, Q. Huang, J. Hazle and C. Li, *ACS Nano*, 2012, **6**, 7489–7496.
129 L. M. Nie, M. Chen, X. L. Sun, P. F. Rong, N. F. Zheng and X. Y. Chen, *Nanoscale*, 2014, **6**, 1271–1276.
130 A. Ray, A. Mukundan, Z. Xie, L. Karamchand, X. Wang and R. Kopelman, *Nanotechnology*, 2014, **25**, 445104.
131 X. Qian, S. Shen, T. Liu, L. Cheng and Z. Liu, *Nanoscale*, 2015, **7**, 6380–6387.
132 L. Cheng, J. Liu, X. Gu, H. Gong, X. Shi, T. Liu, C. Wang, X. Wang, G. Liu, H. Xing, W. Bu, B. Sun and Z. Liu, *Adv. Mater.*, 2014, **26**, 1886–1893.
133 I.-T. Ho, J. L. Sessler, S. S. Gambhir and J. V. Jokerst, *Analyst*, 2015, **140**, 3731–3737.
134 B. Wu, S. T. Lu, H. Yu, R. F. Liao, H. Li, B. V. Lucie Zafitatsimo, Y. S. Li, Y. Zhang, X. L. Zhu, H. G. Liu, H. B. Xu, S. W. Huang and Z. Cheng, *Biomaterials*, 2018, **159**, 37–47.
135 G. Hong, S. Diao, A. L. Antaris and H. Dai, *Chem. Rev.*, 2015, **115**, 10816–10906.
136 D. Kim, M. Lee, Y. D. Suh and S. K. Kim, *J. Am. Chem. Soc.*, 1992, **114**, 4429–4430.
137 V. Krishna, N. Stevens, B. Koopman and B. Moudgil, *Nat. Nanotechnol.*, 2010, **5**, 330–334.
138 P. W. Barone, S. Baik, D. A. Heller and M. S. Strano, *Nat. Mater.*, 2004, **4**, 86–92.
139 M. Pramanik, M. Swierczewska, D. Green, B. Sitharaman and L. V. Wang, *J. Biomed. Opt.*, 2009, **14**, 034018.
140 M. Pramanik, K. H. Song, M. Swierczewska, D. Green, B. Sitharaman and L. V. Wang, *Phys. Med. Biol.*, 2009, **54**, 3291–3301.
141 F. Zhou, S. Wu, Y. Yuan, W. R. Chen and D. Xing, *Small*, 2012, **8**, 1543–1550.
142 J. T. Robinson, S. M. Tabakman, Y. Liang, H. Wang, H. Sanchez Casalongue, D. Vinh and H. Dai, *J. Am. Chem. Soc.*, 2011, **133**, 6825–6831.
143 K. P. Loh, Q. Bao, G. Eda and M. Chhowalla, *Nat. Chem.*, 2010, **2**, 1015–1024.
144 J. Shang, L. Ma, J. Li, W. Ai, T. Yu and G. G. Gurzadyan, *Sci. Rep.*, 2012, **2**, 1–8.
145 M. A. Patel, H. Yang, P. L. Chiu, D. D. T. Mastrogiovanni, C. R. Flach, K. Savaram, L. Gomez, A. Hemnarine,

R. Mendelsohn, E. Garfunkel, H. Jiang and H. He, *ACS Nano*, 2013, **7**, 8147–8157.
146 Z. Sheng, L. Song, J. Zheng, D. Hu, M. He, M. Zheng, G. Gao, P. Gong, P. Zhang, Y. Ma and L. Cai, *Biomaterials*, 2013, **34**, 5236–5243.
147 G. Lalwani, X. Cai, L. Nie, L. V. Wang and B. Sitharaman, *Photoacoustics*, 2013, **1**, 62–67.
148 K. Yang, L. Hu, X. Ma, S. Ye, L. Cheng, X. Shi, C. Li, Y. Li and Z. Liu, *Adv. Mater.*, 2012, **24**, 1868–1872.
149 V. N. Mochalin, O. Shenderova, D. Ho and Y. Gogotsi, *Nat. Nanotechnol.*, 2012, **7**, 11–23.
150 S. Zanganeh, H. Li, P. D. Kumavor, U. Alqasemi, A. Aguirre, I. Mohammad, C. Stanford, M. B. Smith and Q. Zhu, *J. Biomed. Opt.*, 2013, **18**, 096006.
151 G. Wang, F. Zhang, R. Tian, L. Zhang, G. Fu, L. Yang and L. Zhu, *ACS Appl. Mater. Interfaces*, 2016, **8**, 5608–5617.
152 J. Koo, M. Jeon, Y. Oh, H. W. Kang, J. Kim, C. Kim and J. Oh, *Phys. Med. Biol.*, 2012, **57**, 7853–7862.
153 Y.-W. Wang, Y.-Y. Fu, Q. Peng, S.-S. Guo, G. Liu, J. Li, H.-H. Yang and G.-N. Chen, *J. Mater. Chem. B*, 2013, **1**, 5762–5767.
154 K. S. Soppimath, T. M. Aminabhavi, A. R. Kulkarni and W. E. Rudzinski, *J. Controlled Release*, 2001, **70**, 1–20.
155 C. Xie, X. Zhen, Y. Lyu and K. Pu, *Adv. Mater.*, 2017, **29**, 1–7.
156 A. J. Heeger, *Chem. Soc. Rev.*, 2010, **39**, 2354–2371.
157 D. Zhang, M. Wu, Y. Zeng, N. Liao, Z. Cai, G. Liu, X. Liu and J. Liu, *J. Mater. Chem. B*, 2016, **4**, 589–599.
158 Y. Lyu, Y. Fang, Q. Miao, X. Zhen, D. Ding and K. Pu, *ACS Nano*, 2016, **10**, 4472–4481.
159 D. Tuncel and H. V. Demir, *Nanoscale*, 2010, **2**, 484–494.
160 G. Balasundaram, C. J. H. Ho, K. Li, W. Driessen, U. S. Dinish, C. L. Wong, V. Ntziachristos, B. Liu and M. Olivo, *Int. J. Nanomed.*, 2015, **10**, 387–397.
161 Z. Zha, Z. Deng, Y. Li, C. Li, J. Wang, S. Wang, E. Qu and Z. Dai, *Nanoscale*, 2013, **5**, 4462.
162 T. Stahl, R. Bofinger, I. Lam, K. J. Fallon, P. Johnson, O. Ogunlade, V. Vassileva, R. B. Pedley, P. C. Beard, H. C. Hailes, H. Bronstein and A. B. Tabor, *Bioconjugate Chem.*, 2017, **28**, 1734–1740.
163 X. Liang, Y. Li, X. Li, L. Jing, Z. Deng, X. Yue, C. Li and Z. Dai, *Adv. Funct. Mater.*, 2015, **25**, 1451–1462.
164 C. Xie, P. K. Upputuri, X. Zhen, M. Pramanik and K. Pu, *Biomaterials*, 2017, **119**, 1–8.
165 T. Repenko, S. Fokong, L. De Laporte, D. Go, F. Kiessling, T. Lammers and A. J. C. Kuehne, *Chem. Commun.*, 2015, **51**, 6084–6087.
166 X. Cai, X. Liu, L. De Liao, A. Bandla, J. M. Ling, Y. H. Liu, N. Thakor, G. C. Bazan and B. Liu, *Small*, 2016, **12**, 4873–4880.
167 D. Pan, X. Cai, B. Kim, A. J. Stacy, L. V. Wang and G. M. Lanza, *Adv. Healthcare Mater.*, 2012, **1**, 582–589.
168 C. Yin, X. Zhen, Q. Fan, W. Huang and K. Pu, *ACS Nano*, 2017, **11**, 4174–4182.
169 X. Zhen, C. Xie, Y. Jiang, X. Ai, B. Xing and K. Pu, *Nano Lett.*, 2018, **18**, 1498–1505.
170 C. Xie, X. Zhen, Q. Lei, R. Ni and K. Pu, *Adv. Funct. Mater.*, 2017, **27**, 1605397.
171 K. Shou, Y. Tang, H. Chen, S. Chen, L. Zhang, A. Zhang, Q. Fan, A. Yu and Z. Cheng, *Chem. Sci.*, 2018, **9**, 3105–3110.
172 M. Jeon, W. Song, E. Huynh, J. Kim, J. Kim, B. L. Helfield, B. Y. C. Leung, D. E. Goertz, G. Zheng, J. Oh, J. F. Lovell and C. Kim, *J. Biomed. Opt.*, 2014, **8943**, 894321.
173 J. Zhong, S. Yang, X. Zheng, T. Zhou and D. Xing, *Nanomedicine*, 2013, **8**, 903–919.
174 K. Miki, T. Inoue, Y. Kobayashi, K. Nakano, H. Matsuoka, F. Yamauchi, T. Yano and K. Ohe, *Biomacromolecules*, 2015, **16**, 219–227.
175 E. Swider, K. Daoudi, A. H. J. Staal, O. Koshkina, N. Koen Van Riessen, E. Van Dinther, I. Jolanda, M. De Vries, C. L. De Korte and M. Srinivas, *Nanotheranostics*, 2018, **2**, 258–268.
176 S. Sreejith, J. Joseph, M. Lin, N. V. Menon, P. Borah, H. J. Ng, Y. X. Loong, Y. Kang, S. W. K. Yu and Y. Zhao, *ACS Nano*, 2015, **9**, 5695–5704.
177 Q. Fan, K. Cheng, Z. Yang, R. Zhang, M. Yang, X. Hu, X. Ma, L. Bu, X. Lu, X. Xiong, W. Huang, H. Zhao and Z. Cheng, *Adv. Mater.*, 2015, **27**, 843–847.
178 Z. Yang, R. Tian, J. Wu, Q. Fan, B. C. Yung, G. Niu, O. Jacobson, Z. Wang, G. Liu, G. Yu, W. Huang, J. Song and X. Chen, *ACS Nano*, 2017, **11**, 4247–4255.
179 C. Kim, K. H. Song, F. Gao and L. V. Wang, *Radiology*, 2010, **255**, 442–450.
180 K. E. Wilson, S. V. Bachawal and J. K. Willmann, *Clin. Cancer Res.*, 2018, **24**, 3572–3582.
181 A. Garcia-Uribe, T. N. Erpelding, A. Krumholz, H. Ke, K. Maslov, C. Appleton, J. A. Margenthaler and L. V. Wang, *Sci. Rep.*, 2015, **5**, 15748.
182 K. Wilson, K. Homan and S. Emelianov, *Nat. Commun.*, 2012, **3**, 610–618.
183 D. Pan, M. Pramanik, A. Senpan, S. Ghosh, S. A. Wickline, L. V. Wang and G. M. Lanza, *Biomaterials*, 2010, **31**, 4088–4093.
184 D. Pan, M. Pramanik, S. A. Wickline, L. V. Wang and G. M. Lanza, *Contrast Media Mol. Imaging*, 2011, **6**, 378–388.
185 M. F. Kircher, A. De La Zerda, J. V. Jokerst, C. L. Zavaleta, P. J. Kempen, E. Mittra, K. Pitter, R. Huang, C. Campos, F. Habte, R. Sinclair, C. W. Brennan, I. K. Mellinghoff, E. C. Holland and S. S. Gambhir, *Nat. Med.*, 2012, **18**, 829–834.
186 X. Cheng, R. Sun, L. Yin, Z. Chai, H. Shi and M. Gao, *Adv. Mater.*, 2017, **29**, 1604894.
187 J. V. Jokerst, A. J. Cole, D. Van De Sompel, S. S. Gambhir, D. de Sompel, S. S. Gambhir, D. Van De Sompel and S. S. Gambhir, *ACS Nano*, 2012, **6**, 10366–10377.
188 T. Guo, Y. Lin, Z. Li, S. Chen, G. Huang, H. Lin, J. Wang, G. Liu and H.-H. Yang, *Nanoscale*, 2017, **9**, 56–61.
189 Y. Du, Q. Jiang, N. Beziere, L. Song, Q. Zhang, D. Peng, C. Chi, X. Yang, H. Guo, G. Diot, V. Ntziachristos, B. Ding and J. Tian, *Adv. Mater.*, 2016, **28**, 10000–10007.

190 N. Yan, X. Wang, L. Lin, T. Song, P. Sun, H. Tian, H. Liang and X. Chen, *Adv. Funct. Mater.*, 2018, **28**, 1–10.
191 I. Monaco, F. Arena, S. Biffi, E. Locatelli, B. Bortot, F. La Cava, G. M. Marini, G. M. Severini, E. Terreno and M. Comes Franchini, *Bioconjugate Chem.*, 2017, **28**, 1382–1390.
192 M. Jeon, S. Jenkins, J. Oh, J. Kim, T. Peterson, J. Chen and C. Kim, *Nanomedicine*, 2014, **9**, 1377–1388.
193 S. Raveendran, H. T. Lim, T. Maekawa, M. Vadakke Matham and D. Sakthi Kumar, *Nanoscale*, 2018, **10**, 13959–13968.
194 C. Kim, E. C. Cho, J. Chen, K. H. Song, L. Au, C. Favazza, Q. Zhang, C. M. Cobley, F. Gao, Y. Xia and L. V. Wang, *ACS Nano*, 2010, **4**, 4559–4564.
195 C. Bao, J. Conde, F. Pan, C. Li, C. Zhang, F. Tian, S. Liang, J. M. de la Fuente and D. Cui, *Nano Res.*, 2016, **9**, 1043–1056.
196 J. Han, J. Zhang, M. Yang, D. Cui and J. M. de la Fuente, *Nanoscale*, 2016, **8**, 492–499.
197 K. Cheng, S. R. Kothapalli, H. Liu, A. L. Koh, J. V. Jokerst, H. Jiang, M. Yang, J. Li, J. Levi, J. C. Wu, S. S. Gambhir and Z. Cheng, *J. Am. Chem. Soc.*, 2014, **136**, 3560–3571.
198 S. Liang, C. Li, C. Zhang, Y. Chen, L. Xu, C. Bao, X. Wang, G. Liu, F. Zhang and D. Cui, *Theranostics*, 2015, **5**, 970–984.
199 S. K. Maji, S. Sreejith, J. Joseph, M. Lin, T. He, Y. Tong, H. Sun, S. W. K. Yu and Y. Zhao, *Adv. Mater.*, 2014, **26**, 5633–5638.
200 Y. Sheng, L.-D. Liao, N. Thakor and M. C. Tan, *Sci. Rep.*, 2015, **4**, 6562.
201 Z. Sun, Y. Zhao, Z. Li, H. Cui, Y. Zhou, W. Li, W. Tao, H. Zhang, H. Wang, P. K. Chu and X.-F. Yu, *Small*, 2017, **13**, 1602896.
202 C. Sun, L. Wen, J. Zeng, Y. Wang, Q. Sun, L. Deng, C. Zhao and Z. Li, *Biomaterials*, 2016, **91**, 81–89.
203 G. Lv, W. Guo, W. Zhang, T. Zhang, S. Li, S. Chen, A. S. Eltahan, D. Wang, Y. Wang, J. Zhang, P. C. Wang, J. Chang and X. J. Liang, *ACS Nano*, 2016, **10**, 9637–9645.
204 X. R. Song, X. Wang, S. X. Yu, J. Cao, S. H. Li, J. Li, G. Liu, H. H. Yang and X. Chen, *Adv. Mater.*, 2015, **27**, 3285–3291.
205 F. Gong, L. Cheng, N. Yang, Q. Jin, L. Tian, M. Wang, Y. Li and Z. Liu, *Nano Lett.*, 2018, **18**, 6037–6044.
206 D. Pan, X. Cai, C. Yalaz, A. Senpan, K. Omanakuttan, S. A. Wickline, L. V. Wang and G. M. Lanza, *ACS Nano*, 2012, **6**, 1260–1267.
207 Z. Zhou, K. Hu, R. Ma, Y. Yan, B. Ni, Y. Zhang, L. Wen, Q. Zhang and Y. Cheng, *Adv. Funct. Mater.*, 2016, **26**, 5971–5978.
208 S. Park, G. Park, J. Kim, W. Choi, U. Jeong and C. Kim, *Nanoscale*, 2018, **10**, 20548–20558.
209 M. Chen, S. Tang, Z. Guo, X. Wang, S. Mo, X. Huang, G. Liu and N. Zheng, *Adv. Mater.*, 2014, **26**, 8210–8216.
210 K. A. Homan, M. Souza, R. Truby, G. P. Luke, C. Green, E. Vreeland and S. Emelianov, *ACS Nano*, 2012, **6**, 641–650.
211 M. G. Cha, S. Lee, S. Park, H. Kang, S. G. Lee, C. Jeong, Y.-S. Lee, C. Kim and D. H. Jeong, *Nanoscale*, 2017, 12556–12564.
212 W. He, K. Ai, C. Jiang, Y. Li, X. Song and L. Lu, *Biomaterials*, 2017, **132**, 37–47.
213 U. Guler, V. M. Shalaev and A. Boltasseva, *Mater. Today*, 2015, **18**, 227–237.
214 A. De la Zerda, C. Zavaleta, S. Keren, S. Vaithilingam, S. Bodapati, Z. Liu, J. Levi, B. R. Smith, T. J. Ma, O. Oralkan, Z. Cheng, X. Chen, H. Dai, B. T. Khuri-Yakub and S. S. Gambhir, *Nat. Nanotechnol.*, 2008, **3**, 557–562.
215 A. de la Zerda, Z. Liu, S. Bodapati, R. Teed, S. Vaithilingam, B. T. Khuri-Yakub, X. Chen, H. Dai and S. S. Gambhir, *Nano Lett.*, 2010, **10**, 2168–2172.
216 A. De La Zerda, S. Bodapati, R. Teed, S. Y. May, S. M. Tabakman, Z. Liu, B. T. Khuri-Yakub, X. Chen, H. Dai and S. S. Gambhir, *ACS Nano*, 2012, **6**, 4694–4701.
217 D. Chen, C. Wang, X. Nie, S. Li, R. Li, M. Guan, Z. Liu, C. Chen, C. Wang, C. Shu and L. Wan, *Adv. Funct. Mater.*, 2014, **24**, 6621–6628.
218 V. Krishna, A. Singh, P. Sharma, N. Iwakuma, Q. Wang, Q. Zhang, J. Knapik, H. Jiang, S. R. Grobmyer, B. Koopman and B. Moudgil, *Small*, 2010, **6**, 2236–2241.
219 L. Wu, X. Cai, K. Nelson, W. Xing, J. Xia, R. Zhang, A. J. Stacy, M. Luderer, G. M. Lanza, L. V. Wang, B. Shen and D. Pan, *Nano Res.*, 2013, **6**, 312–325.
220 F. Wu, H. Su, Y. Cai, W.-K. Wong, W. Jiang and X. Zhu, *ACS Appl. Bio Mater.*, 2018, **1**, 110–117.
221 T. Zhang, H. Cui, C.-Y. Fang, L.-I. Su, S. Ren, H.-C. Chang, X. Yang and M. Laird Forrest, *J. Biomed. Opt.*, 2013, **18**, 026018.
222 K. Pu, A. J. Shuhendler, J. V. Jokerst, J. Mei, S. S. Gambhir, Z. Bao and J. Rao, *Nat. Nanotechnol.*, 2014, **9**, 233–239.
223 K. Pu, J. Mei, J. V. Jokerst, G. Hong, A. L. Antaris, N. Chattopadhyay, A. J. Shuhendler, T. Kurosawa, Y. Zhou, S. S. Gambhir, Z. Bao and J. Rao, *Adv. Mater.*, 2015, **27**, 5184–5190.
224 E. Huynh, B. Y. C. Leung, B. L. Helfield, M. Shakiba, J. A. Gandier, C. S. Jin, E. R. Master, B. C. Wilson, D. E. Goertz and G. Zheng, *Nat. Nanotechnol.*, 2015, **10**, 325–332.
225 Y. Lyu, X. Zhen, Y. Miao and K. Pu, *ACS Nano*, 2017, **11**, 358–367.
226 Y. Jiang, P. K. Upputuri, C. Xie, Y. Lyu, L. Zhang, Q. Xiong, M. Pramanik and K. Pu, *Nano Lett.*, 2017, **17**, 4964–4969.
227 L. Li, A. A. Shemetov, M. Baloban, P. Hu, L. Zhu, D. M. Shcherbakova, R. Zhang, J. Shi, J. Yao, L. V. Wang and V. V. Verkhusha, *Nat. Commun.*, 2018, **9**, 1–14.
228 J.-W. Kim, E. I. Galanzha, E. V. Shashkov, H.-M. Moon and V. P. Zharov, *Nat. Nanotechnol.*, 2009, **4**, 688–694.
229 X. Liu, C. Lee, W.-C. Law, D. Zhu, M. Liu, M. Jeon, J. Kim, P. N. Prasad, C. Kim and M. T. Swihart, *Nano Lett.*, 2013, **13**, 4333–4339.
230 C. Wang, C. Bao, S. Liang, H. Fu, K. Wang, M. Deng, Q. Liao and D. Cui, *Nanoscale Res. Lett.*, 2014, **9**, 264.

231 H. Moon, H. H. Kim, D. Kumar, H. H. Kim, C. Sim, J. H. Chang, J. M. Kim and D. K. Lim, *ACS Nano*, 2015, **9**, 2711–2719.
232 S. Gao, L. Zhang, G. Wang, K. Yang, M. Chen, R. Tian, Q. Ma and L. Zhu, *Biomaterials*, 2016, **79**, 36–45.
233 Y.-S. Chen, S. J. Yoon, W. Frey, M. Dockery and S. Emelianov, *Nat. Commun.*, 2017, **8**, 15782.
234 I. Monaco, P. Armanetti, E. Locatelli, A. Flori, M. Maturi, S. Del Turco, L. Menichetti and M. Comes Franchini, *J. Mater. Chem. B*, 2018, **6**, 2993–2999.
235 S. Sharifi, S. Behzadi, S. Laurent, M. Laird Forrest, P. Stroeve and M. Mahmoudi, *Chem. Soc. Rev.*, 2012, **41**, 2323–2343.
236 X. Liu, M. Atwater, J. Wang and Q. Huo, *Colloids Surf., B*, 2007, **58**, 3–7.
237 K. Park, S. Biswas, S. Kanel, D. Nepal and R. A. Vaia, *J. Phys. Chem. C*, 2014, **118**, 5918–5926.
238 F. Schöppler, C. Mann, T. C. Hain, F. M. Neubauer, G. Privitera, F. Bonaccorso, D. Chu, A. C. Ferrari and T. Hertel, *J. Phys. Chem. C*, 2011, **115**, 14682–14686.